
Unterschrift BetreuerIn



TECHNISCHE
UNIVERSITÄT
WIEN
Vienna University of Technology

DIPLOMARBEIT

*q*Bounce - Gravity Resonance and Ramsey Spectroscopy

ausgeführt am Atominstitut
der Technischen Universität Wien

unter der Anleitung von
Univ.Prof. Dipl.-Phys. Dr.rer.nat. Hartmut Abele
Dipl.-Ing. Tobias Rechberger

durch

Jakob Micko, BSc
Matr.-Nr.: 1225153

Herbeckstraße 75/7/4, 1180 Wien

May 3, 2018

Unterschrift StudentIn

Abstract

The main goal of this diploma thesis was the supervision and implementation of a setup for a neutron spectrometer. This spectrometer is part of the q BOUNCE experiment and was designed with the neutron and quantum physics group at the Atominstitut in Vienna. The spectrometer itself is located at the Ultra Cold Neutron (UCN) beam line PF2 of the Institut Laue-Langevin (ILL) in Grenoble, France. The goal was to perform Ramsey spectroscopic measurements using UCNs bound in the Earth's gravitational field for the first time. Various calibration measurements were performed, as well as an intermediate measurement with a Rabi spectrometer. I will present a concise overview of the setup and measurements as well as a general theoretic foundation, pertaining to various aspects of the experiment.

Zusammenfassung

Hauptteil dieser Diplomarbeit war die Betreuung und Umsetzung eines Neutronenspektrometers. Das Spektrometer wurde im Rahmen des q BOUNCE Experiments in der Neutronen und Quantenphysik Arbeitsgruppe am Atominstitut der Technischen Universität Wien konstruiert. Standort des Spektrometers ist der Ultra Cold Neutron (UCN) Strahl PF2 am Institut Laue-Langevin (ILL) in Grenoble, Frankreich. Zweck war die Durchführung von Ramsey Spektroskopie Messungen unter Verwendung von UCNs, die im Gravitationsfeld der Erde gebunden sind, was auch gelungen ist. Ebenfalls durchgeführt wurden diverse Kalibrationsmessungen und Messungen mit einem Rabi Spektrometer. In dieser Arbeit gebe ich einen kurzen Überblick über den Aufbau des Neutronenspektrometers und die Kalibrationsmessungen sowie eine theoretische Grundlage der wichtigsten Aspekte des Experiments.

Contents

1	Introduction to Gravity Resonance Spectroscopy	1
1.1	Quantum experiments in Earth's gravitational field	1
1.2	The Quantum Bouncing Ball	2
1.3	Gravity Resonance Spectroscopy	2
1.4	Resonance spectroscopy	2
1.5	Gravity Resonance Spectroscopy using the Ramsey method	5
2	Theory	6
2.1	Energy eigenstates	6
2.2	Oscillating boundary condition	7
2.3	Two state system and Rabi oscillation	11
2.4	Mixed state	13
2.5	Velocity smearing	13
2.6	Ramsey transition	15
3	Measurements during 3-14-358	17
3.1	Background shielding	17
3.2	Aperture	19
3.3	Region I and V	22
3.4	Region II-IV	23
3.5	Leveling	24
3.6	Rabi setup	26
	3.6.1 Driving transitions in the Rabi setup	26
	3.6.2 Measurements and Results	26
4	Conclusio	29
A	Airy functions	32
B	Slit aperture and flight parabola	36

1 Introduction to Gravity Resonance Spectroscopy

Gravitational Resonance Spectroscopy (GRS) applies the methods of resonance spectroscopy in Earth's gravitational field. The transition frequencies of bound states in this field are then analysed using spectroscopic methods which are and have been widely used in many scientific fields. The *q*BOUNCE experiment uses energy transitions of ultra cold neutrons (UCNs), produced at the PF2 instrument at the Institut Laue-Langevin (ILL) in Grenoble, to study their quantum behaviour. The present experiment uses and expands methods of previous experiments, with the goal of increasing accuracy and precision. The *q*BOUNCE group also measures bouncing neutrons above a neutron mirror by analysing the spatial density distribution of propagating neutrons. The GRS method used in the past was the Rabi method and the current iteration of the *q*BOUNCE uses the Ramsey method. This is the logical expansion of the spectrometer, after Rabi measurements. The main thesis work was the supervision of the setup of the Ramsey spectrometer. This was done during two cycles at the ILL. Part of this work was the setup and characterisation of the spectrometer components. Additionally test measurements were done and analysed with parts of the spectrometer. A short theoretical introduction to the theory of GRS is also given in this thesis.

1.1 Quantum experiments in Earth's gravitational field

The first experimental observation of quantum states in the gravitational field was demonstrated in [1, 2]. In this experiment UCNs were confined above a flat surface, a neutron mirror. UCNs are neutrons which are reflected on all surfaces they come into contact with and under all angles [3]. Above the mirror discrete energy eigenstates in the linear gravitational potential should be present. The wave function for UCNs does not enter the mirror significantly which leads to a quantisation of the energy states. The first two eigenstates have an energy of about 1.4 peV and 2.45 peV respectively when compared to the classical energy, as calculated in [4].

The experiment used neutrons as quantum bouncers because the electric polarisability is extremely small when compared to atoms. On top of the mirror an absorber, a rough glass plate, was placed. Between the mirror and the absorber the neutrons propagated. In order to show the discrete nature of the eigen energies of this system, the distance of the absorber to the mirror was varied. If the neutron wave function overlaps with the absorber the neutrons are scattered out of the system, which is the case for higher energy neutrons where the wave function extends farther above the mirror. Lower energy neutrons remain in the system. Using this setup and measuring the transition rate, it was shown for the first time that there are quantised energies and that there is a lowest energy state in the gravitational field, in contrast to a classical system.

One use could be to search for a hypothetical electrical charge of the neutron [5]. By introducing an additional electric field the energies would shift and the charge could be measured. Since the energy resolution is well below the 10 peV range, we plan to lower the upper bound on the neutron charge. For this purpose the Ramsey method needs to be used, described in section 1.5, needs to be used, where the electric field is applied in

the propagation Region of a Ramsey type spectrometer [5].

1.2 The Quantum Bouncing Ball

The experimental methods were further developed and the propagation and evolution of the *bouncing* neutron above a mirror was observed. This bouncing is quantum mechanical in nature and leads to interference effects, which have first been observed in [6, 7, 8]. These bouncing ball experiments were later improved in [9]. Key to this experiment was the development of detectors, which have a spatial resolution in the μm -range [10]. These detectors are ^{10}B coated CR-39 plates, which can reach the desired resolution. This resolution makes the experimental setup uniquely suitable to probe gravitation on small length scales. Especially small scale deviations from Newtonian gravity could be probed, without the residual effects of a charge or polarisation of the measured particle, such as Casimir or Van der Waals forces [11].

1.3 Gravity Resonance Spectroscopy

GRS is a method, where transitions between quantum states in the gravitational potential are induced. The transitions are driven by oscillations of a piezo table. The transition probability is directly related to the driving frequency and the time the oscillation is applied. From this, the difference between energy states can be inferred.

In the linear gravitational potential these energy eigenstates of UCNs above a neutron mirror are separated by different energies, so any transition can be driven, without much interference from other states. The transition probabilities can then be measured via the neutron transmission rate, by measuring only neutrons in the ground state, therefore discarding all excited neutrons. The key to good measurements with this method is to limit external influences, which can introduce large errors, because the measured energies are in the peV range. The basic spectroscopic principles used are resonance methods known from atomic and molecular physics.

1.4 Resonance spectroscopy

The standard tools for spectroscopic experiments are the Rabi and the Ramsey method. They are widely used to investigate transitions in atoms, and are also used in medicine in nuclear magnetic resonance imaging (NMR).

The basis of these methods are two quantum states, $|0\rangle$ and $|1\rangle$, that differ by an energy ΔE . The system starts out in a well defined state and a perturbation is added, to induce transitions.

To visualize this process the *Bloch sphere* is a useful tool. Any two state system can be written as $|\psi\rangle = \cos(\frac{\theta}{2})|0\rangle + \sin(\frac{\theta}{2})e^{i\varphi}|1\rangle$. Using the Pauli matrices the direction of this state in an \mathbb{R}^3 space can be calculated. The expectation value of this direction is given by

$$\langle r \rangle = \begin{pmatrix} \sin(\theta) \cos(\varphi) \\ \sin(\theta) \sin(\varphi) \\ \cos(\theta) \end{pmatrix}. \quad (1)$$

This vector is oriented on the unit sphere with the direction determined by the two angles θ and φ . In NMR this vector can be interpreted as the direction of the spin, whereas in GRS this vector is a useful visualisation of an abstract two state quantum system, with no relation to spin. In spectroscopy perturbations are applied to a quantum system which results in a mixing of the two states and therefore in a change of the state on the Bloch sphere. In GRS these perturbations are induced by mechanical oscillations of the neutron mirror.

If the state starts out in the z -direction and ends in the $-z$ -direction after the perturbation, it is called a “ π -flip”. Similarly when the state ends in the xy -plane it’s called a “ $\frac{\pi}{2}$ -flip”, corresponding to the flip angle on the sphere. Using the time dependent state $|\psi(t)\rangle = \cos(\frac{\theta}{2})e^{-i\omega_0 t} |0\rangle + \sin(\frac{\theta}{2})e^{i\varphi} e^{-i\omega_1 t} |1\rangle$, where $\omega_{0,1} = E_{0,1}/\hbar$, one can separate out the global phase $e^{-i\omega_0 t}$, which leads to $|\psi(t)\rangle = \cos(\frac{\theta}{2}) |0\rangle + \sin(\frac{\theta}{2})e^{i(\varphi - (\omega_1 - \omega_0)t)} |1\rangle$. The vector on the Bloch sphere is then given by

$$\langle r \rangle = \begin{pmatrix} \sin(\theta) \cos(\varphi - (\omega_1 - \omega_0)t) \\ \sin(\theta) \sin(\varphi - (\omega_1 - \omega_0)t) \\ \cos(\theta) \end{pmatrix}, \quad (2)$$

This vector rotates around the z -axis, with an angular frequency that is given by the difference of the energies of the states. In NMR spectroscopy this rotation is directly linked to a precession of the magnetisation and can be measured. In GRS the vector on the Bloch sphere does not correspond to any spin, it is simply a visualisation of the abstract, two state, quantum system.

In spectroscopy, a system with two states is prepared and then a perturbation is applied. One possibility is to apply a π -flip around the y -axis. The duration, the magnitude of the perturbation and the energy difference determines the flip angle, which can be varied by modifying the perturbation until the final state is exactly the second state which corresponds to a π -flip. This is the basic principle of the Rabi spectroscopic method. An example of this type of transition is shown in fig. 1.

It has been shown by Ramsey [12], that the accuracy of this method can be improved, by first applying a $\frac{\pi}{2}$ -flip, then letting the system evolve for a time T without perturbation and then adding a second $\frac{\pi}{2}$ -flip to complete the transition. In spectroscopy this is known as the Ramsey method.

The Ramsey method is generally less susceptible to errors in the specific interaction times used. This is important, for example, if the experimental setup contains a beam of particles, which fly through different regions where the flips and propagation occurs. In this case, the particles have a velocity distribution and therefore the interaction time for different particles, changes. Another benefit of the Ramsey method is that it is less sensitive to an error in the applied perturbation, and is therefore, in a realistic experimental setting, the de facto standard to perform spectroscopic measurements. The downside is, that the Ramsey method can be experimentally more complicated than the Rabi method, since multiple interaction regions have to be realised. The basic procedure can be seen in fig. 2.

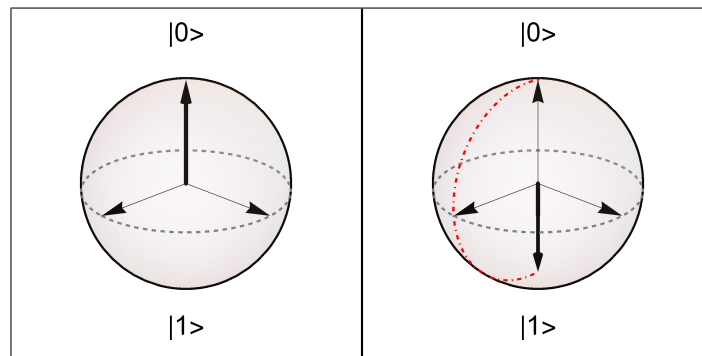


Fig. 1: Bloch sphere showing a π -flip of the initial vector around the y-axis. This transition is used in Rabi spectroscopy.

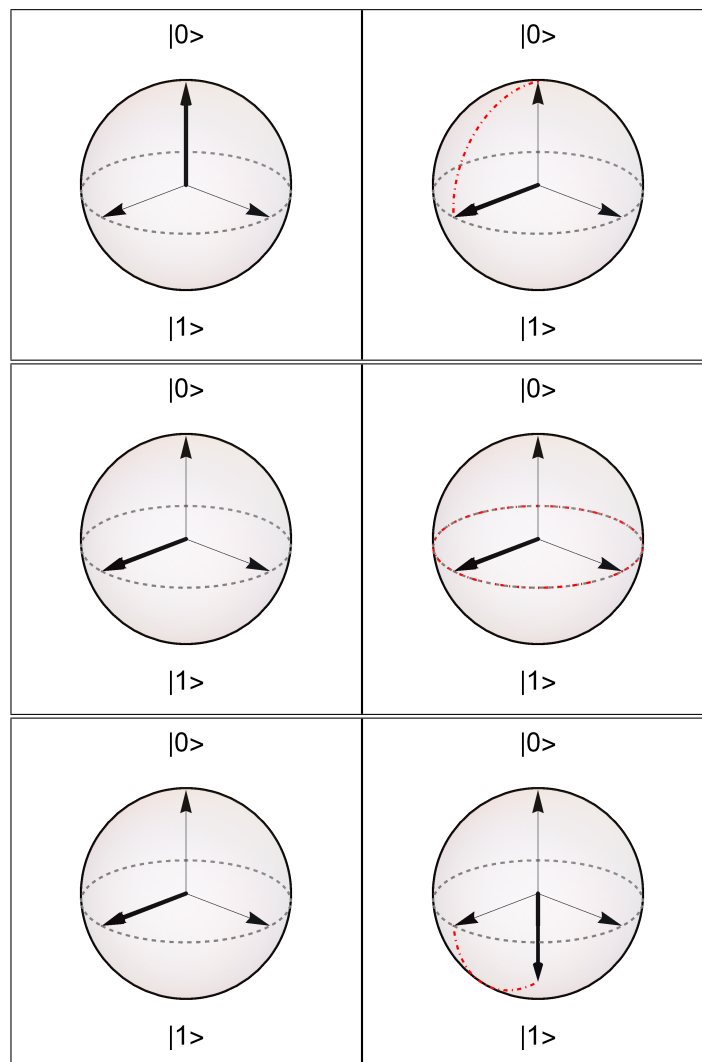


Fig. 2: Bloch sphere showing a $\frac{\pi}{2}$ -flip around the y-Axis in the first line, then a propagation in the second line and then again a $\frac{\pi}{2}$ -flip around the y-axis in the third line. These types of transitions are used in Ramsey spectroscopy.

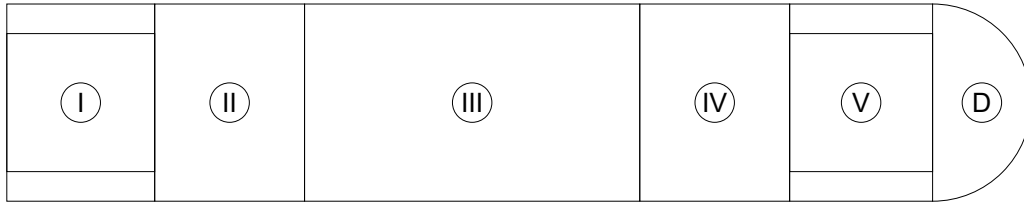


Fig. 3: Schematic of a Ramsey type spectrometer. The neutrons move from left to right. Region I is preparation, II induces the first $\frac{\pi}{2}$ -flip, III is free propagation, IV the second $\frac{\pi}{2}$ -flip, V is the selection of the final state and D is the detector.

1.5 Gravity Resonance Spectroscopy using the Ramsey method

Following the demonstration of Rabi transitions in [13], a setup for GRS using the Ramsey method was now realised for the first time. The main part of this master thesis was the implementation and supervision of the setup of this spectroscopic instrument. The current *q*BOUNCE experiment uses, just like previous iterations, glass mirrors over which the neutrons are bound by the Earth's gravitational potential [1, 2] (also section 2). The schematic of a Ramsey type spectrometer can be seen in fig. 3. The neutrons enter from the left, where there is a slit aperture, which selects UCNs with a specific velocity in flight direction. There are also B_4C mats covering the slot aperture, which shield the spectrometer from neutrons scattering inside the spectroscope without passing the aperture.

In total there are five regions. The first is used to prepare the neutrons in the ground state above the mirror, by scattering all neutrons in excited states. In Region II the mirror is oscillating and thereby inducing transition between energy eigenstates. Region III is used for free propagation. In Region IV the second perturbation is applied. Finally in Region V the neutrons in the ground state are selected. The neutrons are then measured by the detector to the far right. The regions were tested one after the other and the whole spectrometer was built successively. With regions I, II and V a Rabi spectrometer was realised and test measurements with Rabi transitions were made. An analysis of these measurements is done in section 3.6.

2 Theory

A system with neutrons above a surface can be described by a one-dimensional Schrödinger equation. The behaviour in x - and y -direction is not constrained and these two directions can be described by free particle solutions. The Schrödinger equation in z -direction is given by

$$\hat{H} |\psi\rangle = \left(\frac{\hbar^2}{2m} \hat{k}^2 + mg\hat{z} + V_0\Theta(-\hat{z}) \right) |\psi\rangle = i\hbar \frac{d}{dt} |\psi\rangle , \quad (3)$$

where k is the wave vector, m the neutron mass, g the gravitational acceleration, V_0 the Fermi potential of the surface for neutrons and Θ the Heaviside step function. Using the fact that when using UCNs the neutron energy, a few peV, is much smaller than the Fermi energy, about 100 neV, the potential term can be neglected by enforcing the boundary condition, that the solution $|\psi\rangle$ vanishes at the boundary of the surface at $z = 0$. Equation (3) can be cast into a time independent form by assuming a solution of the form $|\psi\rangle = e^{-i\frac{E}{\hbar}t} |\psi_0\rangle$, where $|\psi_0\rangle$ satisfies the time independent equation

$$\hat{H} |\psi_0\rangle = E |\psi_0\rangle . \quad (4)$$

2.1 Energy eigenstates

Using (4) with the Hamiltonian from (3) without the V_0 term one arrives at

$$\left(\frac{\hbar^2}{2m} \hat{k}^2 + mg\hat{z} \right) |\psi_0\rangle = E |\psi_0\rangle . \quad (5)$$

In position space, using $|\psi_0\rangle \rightarrow \psi(z)$, $\hat{k} \rightarrow \frac{1}{i} \frac{d}{dz}$ and $\hat{z} \rightarrow z$, this leads to

$$-\frac{\hbar^2}{2m} \frac{d^2}{dz^2} \psi(z) + mgz\psi(z) = E\psi(z) . \quad (6)$$

By making the substitution $z = z_0\tilde{z}$, with $z_0 = \sqrt[3]{\hbar^2(2m^2g)^{-1}}$, the characteristic length scale for this system, equation (6) reads

$$\left(\frac{d^2}{d\tilde{z}^2} + \left(\frac{E}{mgz_0} - \tilde{z} \right) \right) \psi(\tilde{z}) = 0 . \quad (7)$$

After shifting $\tilde{z} = z' + \frac{E}{mgz_0}$ this results in

$$\left(\frac{d^2}{dz'^2} - z' \right) \psi(z') = 0 , \quad (8)$$

the Airy differential equation. The two solutions to this equation are well known in the literature [14]. They are shown in fig. 4 A derivation of these two solutions is done in appendix A using the Laplace transformation of (8). The physically relevant solution is the solution which goes to zero as $z \rightarrow \infty$ and is known as the Airy Ai function. The diverging solution is called Airy Bi function.

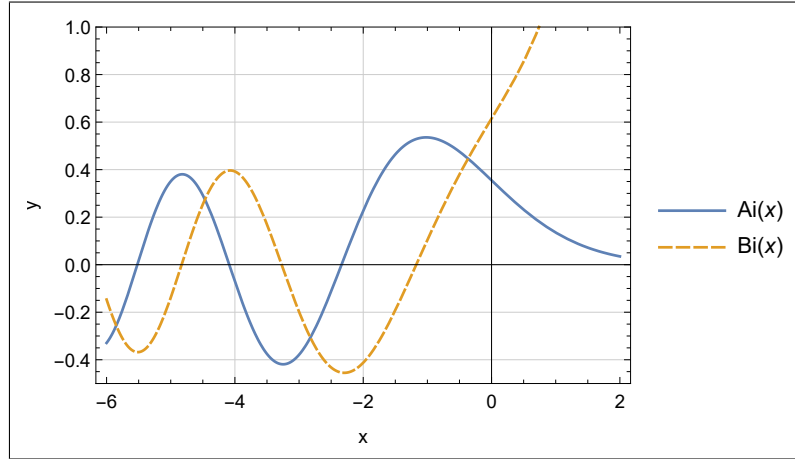


Fig. 4: The two solutions to the Airy differential equation (8).

The solutions to equation (5) need to obey the boundary condition $\psi(0) = 0$ when considering UCNs, so the eigen solutions need to be shifted, such that the zeros of the Airy function coincide with $z = 0$. This boundary condition leads to a quantisation of the allowed energies. From the equation $\tilde{z} = z' + \frac{E}{mgz_0}$ the energy can be calculated. Let ψ_n be the eigenfunction to the energy value E_n where E_0 is the lowest energy state. Then the eigenfunctions can be normalised such that $\int_0^\infty \psi_m^*(z)\psi_n(z)dz = \int_0^\infty \psi_m(z)\psi_n(z)dz = \delta_{mn}$, where the complex conjugation was dropped because the $\psi_n(z)$ can be chosen to be real functions. The first few of these solutions, with their corresponding energies, are shown in fig. 5.

2.2 Oscillating boundary condition

Oscillating boundary conditions have been discussed in [15]. In order to drive transitions between the energy states, the surface, above which the neutrons are bound, is mechanically moved up and down periodically. Using the moving surface, equation (4) has to be modified to

$$i\hbar \frac{d}{dt} |\psi\rangle = \left(\frac{\hbar^2}{2m} \hat{k}^2 + mg\hat{z} + V_0\Theta(a \sin(\omega t + \phi) - \hat{z}) \right) |\psi\rangle \hat{=} \quad (9)$$

$$i\hbar \frac{d}{dt} \psi(z, t) = \left(-\frac{\hbar^2}{2m} \frac{d^2}{dz^2} + mgz + V_0\Theta(a \sin(\omega t + \phi) - z) \right) \psi(z, t),$$

where a is the amplitude and ω the angular frequency of the driving oscillation. Making the substitution $\tilde{z} = z - a \sin(\omega t + \phi)$ and $\tilde{t} = t$, the operators in (9) transform according to $\frac{d}{dz} = \frac{\partial \tilde{z}}{\partial z} \frac{d}{d\tilde{z}} + \frac{\partial \tilde{t}}{\partial z} \frac{d}{d\tilde{t}} = \frac{d}{d\tilde{z}}$ and $\frac{d}{dt} = \frac{\partial \tilde{z}}{\partial t} \frac{d}{d\tilde{z}} + \frac{\partial \tilde{t}}{\partial t} \frac{d}{d\tilde{t}} = -a\omega \cos(\omega \tilde{t} + \phi) \frac{d}{d\tilde{z}} + \frac{d}{d\tilde{t}}$ and the

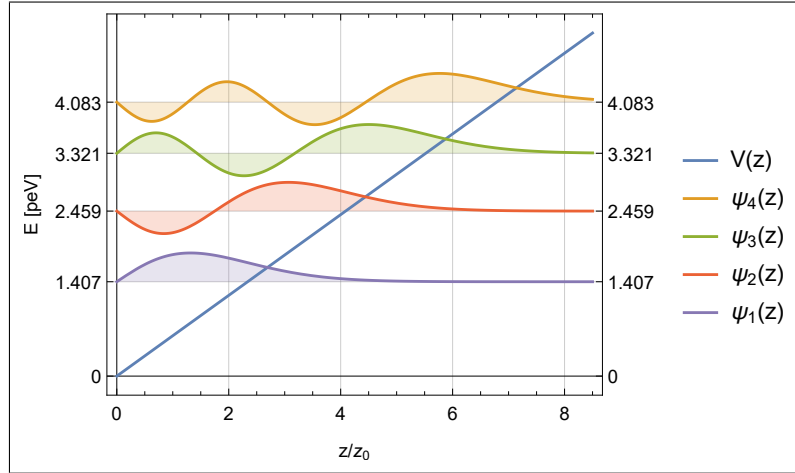


Fig. 5: Time independent bound states in the gravitational potential for neutrons.

equation reads

$$i\hbar \frac{d}{dt} \psi(\tilde{z}, \tilde{t}) = \left(-\frac{\hbar^2}{2m} \frac{d^2}{d\tilde{z}^2} + mg\tilde{z} + V_0 \Theta(-\tilde{z}) + mga \sin(\omega\tilde{t} + \phi) + i\hbar a \omega \cos(\omega\tilde{t} + \phi) \frac{d}{d\tilde{z}} \right) \psi(\tilde{z}, \tilde{t}) . \quad (10)$$

Taking solutions of the time independent equation (5), which satisfy

$$-\frac{\hbar^2}{2m} \frac{d^2}{d\tilde{z}^2} \psi_n(\tilde{z}) + mg\tilde{z} \psi_n(\tilde{z}) = E_n \psi_n(\tilde{z}) \quad (11a)$$

$$\int_0^\infty \psi_m(\tilde{z}) \psi_n(\tilde{z}) d\tilde{z} = \delta_{mn} , \quad (11b)$$

an ansatz for $\psi(\tilde{z}, \tilde{t})$, as a linear combination of these solutions with time dependent coefficients, can be made:

$$\psi(\tilde{z}, \tilde{t}) = \sum_{n=0}^{\infty} C_n(\tilde{t}) e^{-i\frac{E_n}{\hbar}\tilde{t}} \psi_n(\tilde{z}) . \quad (12)$$

m/n	0	1	2	3	4	5
0	0.	97373.5	-53539.9	38301.5	-30393.8	25489.9
1	-97373.5	0.	118935.	-63135.8	44185.7	-34528.6
2	53539.9	-118935.	0.	134572.	-70304.5	48653.3
3	-38301.5	63135.8	-134572.	0.	147213.	-76204.2
4	30393.8	-44185.7	70304.5	-147213.	0.	157984.
5	-25489.9	34528.6	-48653.3	76204.2	-157984.	0.

Tab. 1: The first few components of the interaction potential V_{mn} .

Inserting this into equation (10) leads to

$$\begin{aligned}
& \sum_{n=0}^{\infty} \left(i\hbar e^{-i\frac{E_n}{\hbar}t} \psi_n(\tilde{z}) \dot{C}_n(\tilde{t}) + C_n(\tilde{t}) e^{-i\frac{E_n}{\hbar}t} E_n \psi_n(\tilde{z}) \right) = \\
& = \sum_{n=0}^{\infty} \left(C_n(\tilde{t}) e^{-i\frac{E_n}{\hbar}\tilde{t}} \left(-\frac{\hbar^2}{2m} \frac{d^2}{d\tilde{z}^2} + mg\tilde{z} + V_0 \Theta(-\tilde{z}) \right) \psi_n(\tilde{z}) + \right. \\
& + C_n(\tilde{t}) e^{-i\frac{E_n}{\hbar}\tilde{t}} \left(mga \sin(\omega\tilde{t} + \phi) + i\hbar a \omega \cos(\omega\tilde{t} + \phi) \frac{d}{d\tilde{z}} \right) \psi_n(\tilde{z}) \Big) = \quad (13) \\
& = \sum_{n=0}^{\infty} \left(C_n(\tilde{t}) e^{-i\frac{E_n}{\hbar}\tilde{t}} E_n \psi_n(\tilde{z}) + \right. \\
& + C_n(\tilde{t}) e^{-i\frac{E_n}{\hbar}\tilde{t}} \left(mga \sin(\omega\tilde{t} + \phi) + i\hbar a \omega \cos(\omega\tilde{t} + \phi) \frac{d}{d\tilde{z}} \right) \psi_n(\tilde{z}) \Big) ,
\end{aligned}$$

where, in the second step, (11a) and the boundary condition $\psi(z_0) = 0$ was used. After simplifying, multiplying by $\psi_m(\tilde{z})$, integrating over \tilde{z} and using (11b) this results in

$$\begin{aligned}
i\hbar \dot{C}_m(\tilde{t}) & = e^{i\frac{E_m}{\hbar}\tilde{t}} \sum_{n=0}^{\infty} \left(mga \sin(\omega\tilde{t} + \phi) e^{-i\frac{E_n}{\hbar}\tilde{t}} \delta_{mn} + \right. \\
& + i\hbar a \omega \cos(\omega\tilde{t} + \phi) e^{-i\frac{E_n}{\hbar}\tilde{t}} \int_0^{\infty} \psi_m(\tilde{z}) \frac{d}{d\tilde{z}} \psi_n(\tilde{z}) d\tilde{z} \Big) C_n(\tilde{t}) = \quad (14) \\
& = mga \sin(\omega\tilde{t} + \phi) C_m(\tilde{t}) + \sum_{n=0}^{\infty} \left(i\hbar a \omega \cos(\omega\tilde{t} + \phi) e^{i\frac{E_m - E_n}{\hbar}\tilde{t}} V_{mn} \right) C_n(\tilde{t}) ,
\end{aligned}$$

where $V_{mn} := \int_0^{\infty} \psi_m(\tilde{z}) \frac{d}{d\tilde{z}} \psi_n(\tilde{z}) d\tilde{z} = -V_{nm}$ is antisymmetric. The first few V_{mn} can be seen in tab. 1.

Making another transformation $C_n(\tilde{t}) = f(\tilde{t}) \tilde{C}_n(\tilde{t})$ and $(E_m - E_n)/\hbar := \omega_{mn}$ leads to

$$\begin{aligned}
i\hbar \dot{f}(\tilde{t}) \tilde{C}_m(\tilde{t}) + i\hbar f(\tilde{t}) \dot{\tilde{C}}_m(\tilde{t}) & = mga \sin(\omega\tilde{t} + \phi) f(\tilde{t}) \tilde{C}_m(\tilde{t}) \\
& + \sum_{n=0}^{\infty} \left(i\hbar a \omega \cos(\omega\tilde{t} + \phi) f(\tilde{t}) e^{i\omega_{mn}\tilde{t}} V_{mn} \right) \tilde{C}_n(\tilde{t}) , \quad (15)
\end{aligned}$$

m/n	0	1	2	3	4	5
0	0.	-254.535	-462.925	-647.101	-815.462	-972.345
1	254.535	0.	-208.39	-392.566	-560.927	-717.81
2	462.925	208.39	0.	-184.176	-352.537	-509.42
3	647.101	392.566	184.176	0.	-168.361	-325.244
4	815.462	560.927	352.537	168.361	0.	-156.883
5	972.345	717.81	509.42	325.244	156.883	0.

Tab. 2: The first few transition frequencies $\omega_{mn}/2\pi$.

where the first few transition frequencies $\omega_{mn}/2\pi$ can be seen in tab. 2.

With the requirement $i\hbar\dot{f}(\tilde{t}) = mga \sin(\omega\tilde{t} + \phi)f(\tilde{t})$ it follows that $f(\tilde{t}) = e^{i\frac{mga}{\hbar\omega} \cos(\omega\tilde{t} + \phi)}$ and equation (15) simplifies to

$$\dot{\tilde{C}}_m = a\omega \cos(\omega\tilde{t} + \phi) \sum_{n=0}^{\infty} e^{i\omega_{mn}\tilde{t}} V_{mn} \tilde{C}_n(\tilde{t}). \quad (16)$$

Taking the complex conjugate leads to

$$\dot{\tilde{C}}_m^*(\tilde{t}) = a\omega \cos(\omega\tilde{t} + \phi) \sum_{n=0}^{\infty} e^{-i\omega_{mn}\tilde{t}} V_{mn} \tilde{C}_n^*(\tilde{t}), \quad (17)$$

since the V_{mn} are purely real. Then equations (16) and (17) can be combined to give

$$\begin{aligned} \frac{d}{dt} \left(\tilde{C}_m(\tilde{t}) \tilde{C}_n^*(\tilde{t}) \right) &= \dot{\tilde{C}}_m(\tilde{t}) \tilde{C}_n^*(\tilde{t}) + \tilde{C}_m(\tilde{t}) \dot{\tilde{C}}_n^*(\tilde{t}) = \\ &= \sum_{l=0}^{\infty} \left(a\omega \cos(\omega\tilde{t} + \phi) e^{i\omega_{ml}\tilde{t}} V_{ml} \tilde{C}_l(\tilde{t}) \tilde{C}_n^*(\tilde{t}) + \tilde{C}_m(\tilde{t}) \tilde{C}_l^*(\tilde{t}) a\omega \cos(\omega\tilde{t} + \phi) e^{-i\omega_{nl}\tilde{t}} V_{nl} \right) = \\ &= \sum_{l=0}^{\infty} \left(a\omega \cos(\omega\tilde{t} + \phi) e^{i\omega_{ml}\tilde{t}} V_{ml} \tilde{C}_l(\tilde{t}) \tilde{C}_n^*(\tilde{t}) - \tilde{C}_m(\tilde{t}) \tilde{C}_l^*(\tilde{t}) a\omega \cos(\omega\tilde{t} + \phi) e^{i\omega_{ln}\tilde{t}} V_{ln} \right), \end{aligned} \quad (18)$$

where, in the second equality, the antisymmetry of ω_{mn} and V_{mn} was used. Defining the density matrix $\rho_{mn} = \tilde{C}_m(\tilde{t}) \tilde{C}_n^*(\tilde{t})$ and also $U_{ml} = a\omega \cos(\omega\tilde{t} + \phi) e^{i\omega_{ml}\tilde{t}} V_{ml}$ (leaving the time dependence implicit) this can be concisely written as

$$\dot{\rho}_{mn} = \sum_{l=0}^{\infty} (U_{ml} \rho_{ln} - \rho_{ml} U_{ln}). \quad (19)$$

The probability to be in a state $\chi = \sum_{i=0}^{\infty} a_i \psi_i(\tilde{z})$ is given by

$$P(\chi) = \sum_{i=0, j=0}^{\infty} a_i \tilde{C}_i^*(\tilde{t}) a_j^* \tilde{C}_j(\tilde{t}) = \sum_{i=0, j=0}^{\infty} a_i a_j^* \tilde{C}_j(\tilde{t}) \tilde{C}_i^*(\tilde{t}) = \sum_{i=0, j=0}^{\infty} a_i a_j^* \rho_{ji}. \quad (20)$$

Defining $\rho_{ij}^a = a_i a_j^*$, this can be written as

$$P(\rho^a) = \sum_{i=0, j=0}^{\infty} \rho_{ij}^a \rho_{ji} = \text{Tr}(\rho^a \rho), \quad (21)$$

where, in the last step, ρ_{ij}^a and ρ_{ji} are used as matrices and Tr is the trace of the resulting matrix. This is the probability of finding a state with density matrix ρ in the state with density matrix ρ^a .

2.3 Two state system and Rabi oscillation

Equation (16) can not be solved exactly in all generality. One simplification is to only take into account two states where the state 0 is the lower energy state and state 1 the higher energy state, so that $\omega_{10} > 0$. Then (16) can be written as a matrix equation

$$\begin{aligned} \begin{pmatrix} \dot{\tilde{C}}_0(\tilde{t}) \\ \dot{\tilde{C}}_1(\tilde{t}) \end{pmatrix} &= \begin{pmatrix} 0 & a\omega \cos(\omega\tilde{t} + \phi) e^{i\omega_{01}\tilde{t}} V_{01} \\ a\omega \cos(\omega\tilde{t} + \phi) e^{i\omega_{10}\tilde{t}} V_{10} & 0 \end{pmatrix} \begin{pmatrix} \tilde{C}_0(\tilde{t}) \\ \tilde{C}_1(\tilde{t}) \end{pmatrix} \\ &= \begin{pmatrix} 0 & a\omega \cos(\omega\tilde{t} + \phi) e^{-i\omega_{10}\tilde{t}} V_{01} \\ -a\omega \cos(\omega\tilde{t} + \phi) e^{i\omega_{10}\tilde{t}} V_{01} & 0 \end{pmatrix} \begin{pmatrix} \tilde{C}_0(\tilde{t}) \\ \tilde{C}_1(\tilde{t}) \end{pmatrix}, \end{aligned} \quad (22)$$

where the antisymmetry of V_{mn} and ω_{mn} has been used. To solve this equation an additional approximation has to be made. The term $\cos(\omega\tilde{t} + \phi) e^{-i\omega\tilde{t}} = \frac{1}{2} (e^{i((\omega-\omega_{10})\tilde{t} + \phi)} + e^{-i((\omega+\omega_{10})\tilde{t} + \phi)})$ can be approximated by $\frac{e^{i((\omega-\omega_{10})\tilde{t} + \phi)}}{2}$. The faster oscillating term is assumed to have little effect on the total evolution of the system, since these terms average to zero fast when compared to the slower oscillating term. A similar argument is used for the second term in the matrix equation. This leads to the equation

$$\begin{pmatrix} \dot{\tilde{C}}_0(\tilde{t}) \\ \dot{\tilde{C}}_1(\tilde{t}) \end{pmatrix} = \begin{pmatrix} 0 & \frac{a\omega}{2} e^{i(\tilde{\omega}\tilde{t} + \phi)} V_{01} \\ -\frac{a\omega}{2} e^{-i(\tilde{\omega}\tilde{t} + \phi)} V_{01} & 0 \end{pmatrix} \begin{pmatrix} \tilde{C}_0(\tilde{t}) \\ \tilde{C}_1(\tilde{t}) \end{pmatrix}, \quad (23)$$

where $\tilde{\omega} := \omega - \omega_{10}$. The coefficient matrix in this equation can be made time independent by the further substitutions $\tilde{C}_0(\tilde{t}) = e^{i\frac{\tilde{\omega}\tilde{t} + \phi}{2}} C'_0(\tilde{t})$ and $\tilde{C}_1(\tilde{t}) = e^{-i\frac{\tilde{\omega}\tilde{t} + \phi}{2}} C'_1(\tilde{t})$, resulting in

$$\begin{pmatrix} \dot{C}'_0(\tilde{t}) \\ \dot{C}'_1(\tilde{t}) \end{pmatrix} = \begin{pmatrix} -i\frac{\tilde{\omega}}{2} & \frac{a\omega}{2} V_{01} \\ -\frac{a\omega}{2} V_{01} & i\frac{\tilde{\omega}}{2} \end{pmatrix} \begin{pmatrix} C'_0(\tilde{t}) \\ C'_1(\tilde{t}) \end{pmatrix}. \quad (24)$$

This equation can be solved by diagonalisation. After defining $r \cos(\Omega) := |\frac{\tilde{\omega}}{2}|$ and $r \sin(\Omega) := |\frac{a\omega}{2} V_{01}|$ so that $r = \sqrt{(\frac{\tilde{\omega}}{2})^2 + (\frac{a\omega}{2} V_{01})^2}$, the eigenvalues of the matrix in (24) are $\pm ir$. The corresponding eigenvectors are

$$v_{ir} = \begin{pmatrix} \sin(\frac{\Omega}{2}) \\ i \cos(\frac{\Omega}{2}) \end{pmatrix}, \quad v_{-ir} = \begin{pmatrix} \cos(\frac{\Omega}{2}) \\ -i \sin(\frac{\Omega}{2}) \end{pmatrix} \quad (25)$$

and the solution to (24) can be written as

$$\begin{aligned} \begin{pmatrix} C'_0(\tilde{t}) \\ C'_1(\tilde{t}) \end{pmatrix} &= \alpha e^{ir\tilde{t}} v_{ir} + \beta e^{-ir\tilde{t}} v_{-ir} = \\ &= \begin{pmatrix} \cos(r\tilde{t}) - i \sin(r\tilde{t}) \cos \Omega & \sin(r\tilde{t}) \sin(\Omega) \\ -\sin(r\tilde{t}) \sin(\Omega) & \cos(r\tilde{t}) + i \sin(r\tilde{t}) \cos \Omega \end{pmatrix} \begin{pmatrix} C'_0(0) \\ C'_1(0) \end{pmatrix}, \end{aligned} \quad (26)$$

where α and β are constants. With this, the final solution to (12) is given by

$$\begin{aligned} \psi(\tilde{z}, \tilde{t}) &= e^{i\frac{mga}{\hbar\omega}(\cos(\omega\tilde{t}+\phi)-\cos(\phi))} \\ &((\cos(r\tilde{t}) - i \sin(r\tilde{t}) \cos(\Omega))C_0(0) + \sin(r\tilde{t}) \sin(\Omega)e^{i\phi}C_1(0))e^{i(\frac{\tilde{\omega}}{2}-\frac{E_0}{\hbar})\tilde{t}}\psi_0(\tilde{z}) + \\ &+ ((\cos(r\tilde{t}) + i \sin(r\tilde{t}) \cos(\Omega))C_1(0) - \sin(r\tilde{t}) \sin(\Omega)e^{-i\phi}C_0(0))e^{-i(\frac{\tilde{\omega}}{2}+\frac{E_1}{\hbar})\tilde{t}}\psi_1(\tilde{z}) = \\ &t_0(\tilde{t}, \phi)\psi_0(\tilde{z}) + t_1(\tilde{t}, \phi)\psi_1(\tilde{z}), \end{aligned} \quad (27)$$

with

$$\begin{aligned} t_0(\tilde{t}, \phi) &= e^{i\frac{mga}{\hbar\omega}(\cos(\omega\tilde{t}+\phi)-\cos(\phi))} \\ &((\cos(r\tilde{t}) - i \sin(r\tilde{t}) \cos(\Omega))C_0(0) + \sin(r\tilde{t}) \sin(\Omega)e^{i\phi}C_1(0))e^{i(\frac{\tilde{\omega}}{2}-\frac{E_0}{\hbar})\tilde{t}} \\ t_1(\tilde{t}, \phi) &= e^{i\frac{mga}{\hbar\omega}(\cos(\omega\tilde{t}+\phi)-\cos(\phi))} \\ &((\cos(r\tilde{t}) + i \sin(r\tilde{t}) \cos(\Omega))C_1(0) - \sin(r\tilde{t}) \sin(\Omega)e^{-i\phi}C_0(0))e^{-i(\frac{\tilde{\omega}}{2}+\frac{E_1}{\hbar})\tilde{t}}. \end{aligned} \quad (28)$$

From this the probability of finding a neutron in the state $\psi_m(\tilde{z})$ can be extracted via

$$P(\psi_m) = \left| \int_0^\infty \psi_m^*(\tilde{z})\psi(\tilde{z})d\tilde{z} \right|^2, \quad (29)$$

where property (11b) is useful. Taking the definition $\Omega = \arccos(\frac{a\omega V_{01}}{2r})$ it is clear that this is unsymmetric with respect to the resonant frequency ω_{10} , since $r =$

$\sqrt{(\frac{\tilde{\omega}}{2})^2 + (\frac{a\omega}{2}V_{01})^2}$. This asymmetry can be removed by using the maximum velocity of the oscillation, $a\omega$, as the parameter defining the perturbation rather than the maximum displacement a . For example when considering the transition from the first to the second energy eigenstate, $\omega_{10} \approx 1599.29 \approx 2\pi \cdot 254.53$, $V_{01} = 97373.5$ and a velocity of $a\omega = 10^{-3}$, the transition probability from state $\psi_0 \rightarrow \psi_1$ is given by

$$P(\psi_1) = \left| \cos(r\tilde{t}) - i \sin(r\tilde{t}) \cos(\Omega) \right|^2 = 1 - \sin^2(r\tilde{t}) \sin^2(\Omega), \quad (30)$$

and can be seen in fig. 6 where the interaction time $\tilde{t} = \frac{0.152}{8.878} = 0.0171$ s corresponds to the one for the most probable velocity (see section 3.2). The probability for a transition $\psi_0 \rightarrow \psi_1$ is shown as the solid orange line. If the initial state is not a pure state but a mixture between ψ_0 and ψ_1 , the transition probabilities have to be calculated by squaring the general transition amplitudes t_i defined in equation (27). The probability of finding the system to be in a certain state is given by

$$\begin{aligned} P(\psi_0) &= |t_0|^2 \\ P(\psi_1) &= |t_1|^2. \end{aligned} \quad (31)$$

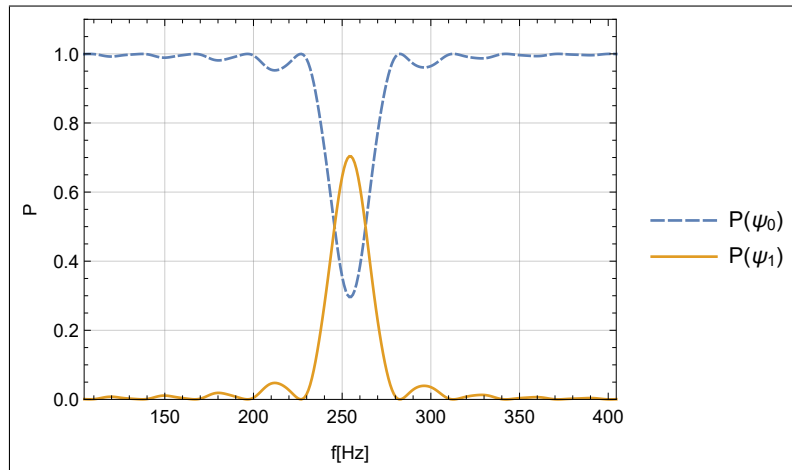


Fig. 6: Example of transition probabilities between two states with the same perturbation time as was used in the experiment.

2.4 Mixed state

When using the same values as in fig.6 but with the occupation numbers $C_0(0) = \sqrt{\frac{2}{3}}$ and $C_1(0) = \sqrt{\frac{1}{3}}$, the transition probabilities can be seen in fig.7. This reduces the contrast of the transition, which requires more accurate measurements.

2.5 Velocity smearing

All the previous plots were calculated with the most probable velocity of the PF2 UCNs. In the experiment the interaction time is given by the velocity of the neutrons and the length of the interaction region. The interaction region has a length of 152 mm. Using the velocity spectrum, given in section 3.2, the transition probabilities are given by

$$\begin{aligned} \langle P(\psi_0) \rangle &= \int P(\psi_0|v)\rho(v)dv \\ \langle P(\psi_1) \rangle &= \int P(\psi_1|v)\rho(v)dv, \end{aligned} \tag{32}$$

where the $P(\psi_i|v)$ are from equations (31) and $v = \frac{0.152}{t}$ is explicitly displayed. These can not be given in analytical form, since the velocity distribution is not known in closed form. Averaging the transition probabilities in fig. 7 over the velocities results in fig. 8. This causes a reduction in the side bands and the width of the transition. In the experiment the vibrational amplitude is fixed and the perturbation varies only with the interaction times and therefore with the velocities. This causes some transition peaks to lose more details than others.

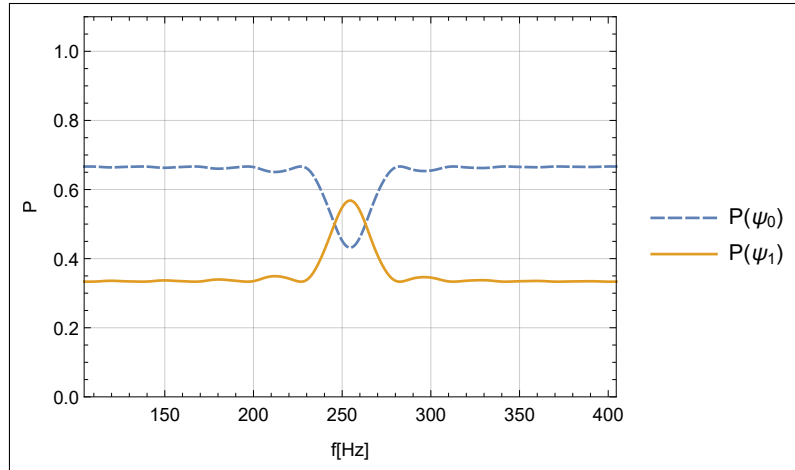


Fig. 7: Transition probabilities for a mixed state with $C_0(0) = \sqrt{\frac{2}{3}}$ and $C_1(0) = \sqrt{\frac{1}{3}}$.

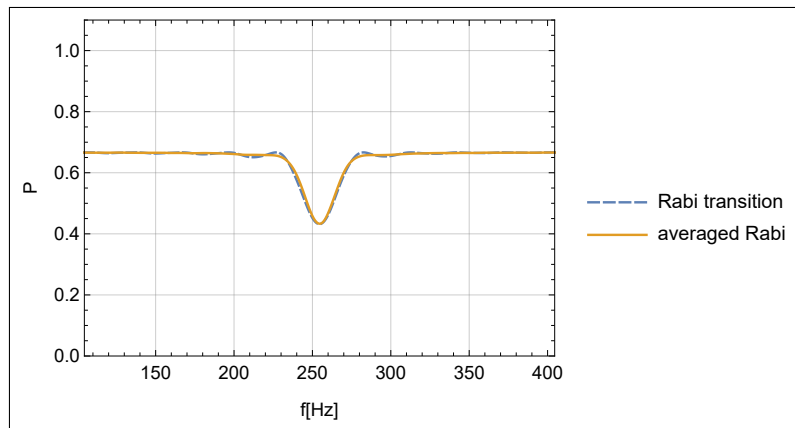


Fig. 8: Velocity averaged Rabi transition for a mixed state.

2.6 Ramsey transition

The basis for the Ramsey method is to split the interaction in two separate parts. Unlike with the Rabi method with a single π -flip, there are two perturbation regions. In each region a $\frac{\pi}{2}$ -flip is applied. Between the two flips, the system is allowed to propagate freely. This leads to sharper transition peaks, as can be seen in fig. 9. Using this method can greatly increase the accuracy with which the transition frequency can be determined. The width of the Ramsey fringes is dependent on the propagation between the two interaction regions. As with the Rabi method, the transmission spectrum gets washed out when averaging over the velocity distribution. This can be seen in fig. 10. The first maxima in the probability around the central minimum are still clearly visible and can be used to determine the transition frequency more accurately than with the Rabi method. This makes the Ramsey method a very versatile tool for spectroscopy. One drawback is the more complicated experimental setup, where two interaction regions and a propagation region are needed. The lengths of regions II, III and IV of the GRS Ramsey setup are 152 mm, 340 mm and again 152 mm.

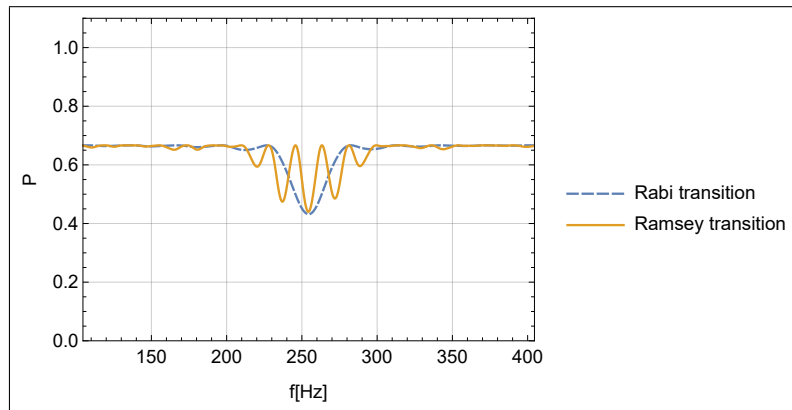


Fig. 9: Rabi transition in comparison with a Ramsey transition.

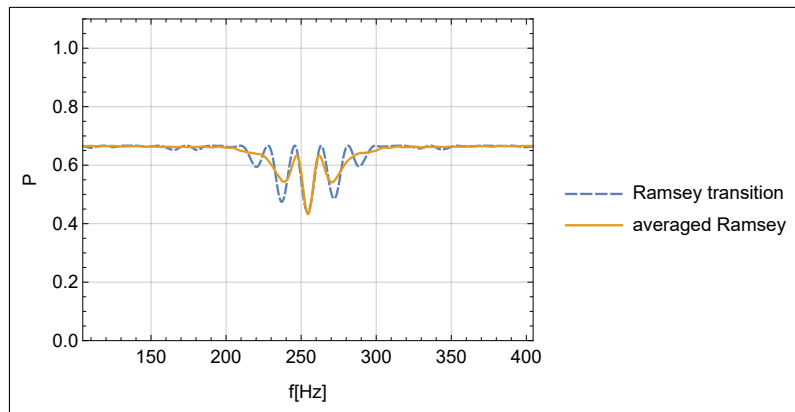


Fig. 10: Ramsey transition in comparison to the same transition averaged over a velocity spectrum.

3 Measurements during 3-14-358

The experiment consists of a vacuum chamber, lined with μ -metal, to suppress the ambient magnetic field. Inside the chamber, there is an optical table made from granite. On this table the rest of the setup is placed. On one end of the vacuum chamber (henceforth called “front”) there is a beam guide and the turbo molecular pump, and on the other end (“back”) there are various feedthroughs for the cables of different components. There are components to maintain a level granite table, measure the relative position of the mirrors, piezos to position and oscillate the mirrors and laser interferometers to monitor the movement of the mirrors. The beam guide in the front comes directly from the UCN source at the ILL, and enters the vacuum chamber. At the end of the beam guide there is an end cap with an aluminium window. This window is in a height of about 79 mm above and positioned in the middle of the granite table. Then there is a slit aperture to select neutrons of a certain velocity in flight direction. Around the window and aperture, there is a box made of B_4C , to reduce background neutrons. After this the five regions of the spectrometer follow.

After the aperture, the first neutron mirror, Region I, is placed. Above Region I there is a glass absorber to prepare the neutrons in the initial state. Then follows the second mirror, Region II, mounted on a piezo, in order to induce oscillations. These oscillations are controlled by a function generator and drive the transitions between energy states. Region III, a longer, stationary, neutron mirror is used for the undisturbed propagation. Region IV is again controlled by the function generator to drive transitions. Lastly Region V, again with an absorber, selects the final state. Finally there is the detector to measure the transition rate. Above the spectrometer mirrors there is an aluminium structure, to support movable holders for sensors. There are sensors to measure the mirror position and the remaining magnetic field, as well as mirrors for laser interferometers to check the oscillation amplitudes and frequencies during the experiment.

3.1 Background shielding

To reduce unwanted background neutrons a shielding consisting of B_4C mats was built around the beam guide and the aperture. This can be seen in fig. 11 to the far left in black. A schematic view from the top is shown in fig. 12. The main purpose is to reduce direct paths from the end of the beam guide to the detector. Test measurements with the detector in the neutron path, with no mirrors between detector and aperture and with a blocked aperture resulted in tab. 3. In this table, background means the neutron rate with no neutrons entering the spectrometer. This rate is measured to correct for global variations of the neutron background, unrelated to the experiment. The neutron flight path was blocked by a sheet of aluminium and tape. These measurements showed that neutrons which enter the detector do fly through the opening in the shielding and are not scattered into the detector from somewhere else in the vacuum chamber.

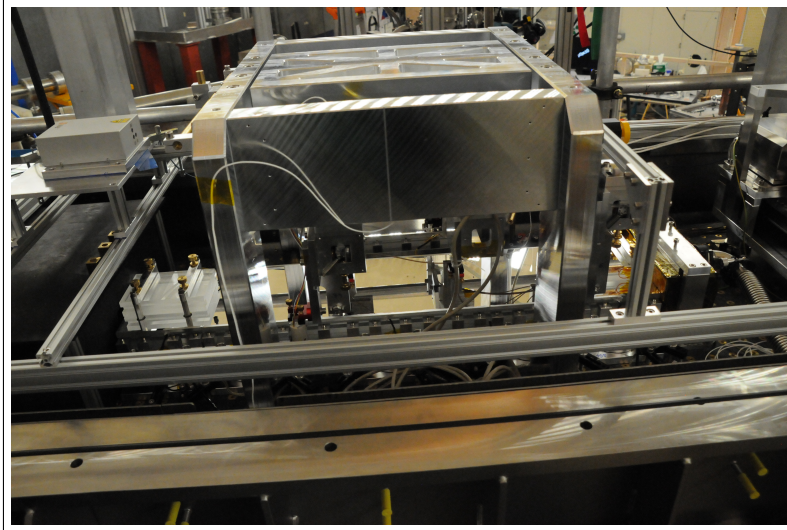


Fig. 11: The final spectrometer with all essential features.

Measurement	Rate	Background
Unblocked	(222.97 ± 0.21) Hz	(0.14 ± 0.01) Hz
Blocked	(0.34 ± 0.13) Hz	(0 ± 0) Hz

Tab. 3: Rates as measured behind the shielding. The second measurement is with a blocked neutron path.

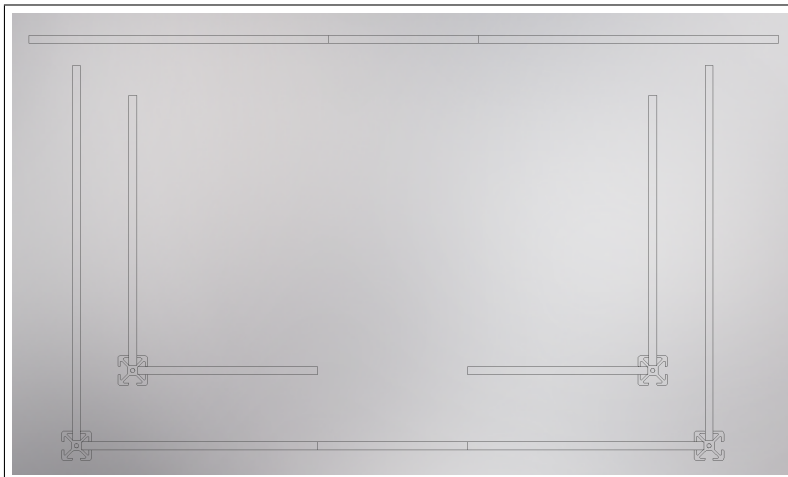


Fig. 12: Schematic of the placement of the B_4C mats, as shielding. The slit aperture is placed in the space in the middle. The neutrons enter from the top and fly down, where the ramsey spectrometer follows.

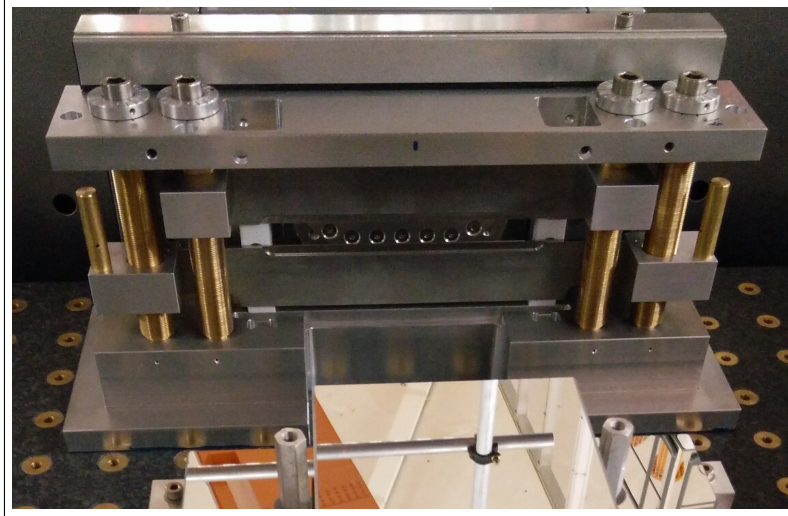


Fig. 13: Image of the slit aperture.

3.2 Aperture

The aperture consists of two independently movable plates, made of boronated steel, which can be positioned to create a slit aperture (see fig. 13). The upper and lower slit plates can be adjusted using the micrometer screws seen on top. This slit is used to select a velocity component in the horizontal flight direction. To estimate the velocity of the neutrons, the classical flight path of a point particle in a homogeneous gravitational field is considered. The trajectory can then be described by a parabola. As an approximation, it is assumed that the absorber above Region I is so close that the parabola has its vertex exactly at the surface of the mirror (see fig. 14). An analysis of this approximation is done in appendix B. The parabola also has to intercept the surface of the first mirror, which uniquely fixes the flightpath. Using v_z and v_x as the velocities in x - and z -direction at the time $t = 0$ and g as the gravitational acceleration of the Earth, the motion of the particle is given by

$$\begin{aligned} z(t) &= v_z t - \frac{g}{2} t^2 \\ x(t) &= v_x t \end{aligned} \tag{33}$$

Using the fact that the vertex of the parabola has to be at the height h of the mirror surface it follows that $v_z = \sqrt{2hg}$. Inserting this into (33) and using, that the vertex also has to be at a distance d from the origin, the velocity in flight direction is given by $v_x = d\sqrt{\frac{g}{2h}}$. From this the velocity in flight direction is limited from below by the lower aperture plate and from above by the upper plate. The calculation is classical and quantum mechanical corrections are not taken into account. These calculations are only used to make rough estimations of the velocity, since there are many effects not taken into account. Using these approximate results, the neutron velocity spectrum was

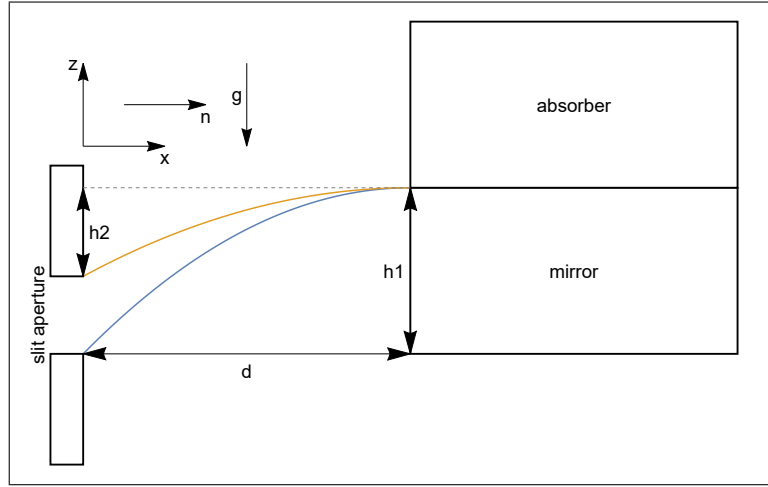


Fig. 14: Schematic illustration of the classical parabolas used to estimate the velocity distribution of the neutron beam, in flight direction. The lower aperture plate limits the lower velocity, and the upper plate the upper velocity.

characterised. To do this the slit was opened to let a velocity window of 1 m/s pass, and the velocity was swept from 3 m/s to 15 m/s. By detecting the neutron rate after the mirror and the absorber, the velocity spectrum was estimated. One correction taken into account is that the distances to the mirror, from the upper and lower aperture plates, are not equal. The upper plate is at a distance of $d_u = (164.912 \pm 0.020)$ mm and the lower at $d_l = (164.568 \pm 0.020)$ mm. From this the aperture slit heights above the granite can be calculated and were measured to within 0.01 mm. The calculated values can be seen in tab. 4 with corresponding errors for the upper and the lower velocities.

The velocity spectrum from these measurements can be seen in fig. 15, where count rate over velocity is plotted. The corresponding values and probabilities can be seen in tab. 5. From this the expected velocity is given by $\langle v \rangle = (8.878 \pm 0.108)$ m/s. The neutron velocity controls the time a neutron is in the interferometer and therefore also the interaction time with the perturbation. This ultimately influences the achievable contrast. With this in mind, the velocity window should be as narrow as possible, optimised for the mirror length and the peak of the neutron intensity. However, since the count rate is very low at the end of the spectrometer, the velocity window should be as large as possible. With these two competing criteria, the final slit positions were chosen to be $h_l = 99.61$ mm for the lower plate and $h_u = (104.21 \pm 0.01)$ mm for the upper plate, which correspond to an velocity interval from $v_{\min} = (4.630 \pm 0.015)$ m/s to $v_{\max} = (12.99 \pm 0.27)$ m/s. The selected velocities are shown in orange in fig. 15. The errors of the velocities are estimated assuming an accuracy of all the height and distance measurements of 0.01 mm and an additional error of $\Delta h_{\text{absorber}} \approx 0.03$ mm in height, because the absorber is not exactly above the mirror (see section 3.3). An additional analysis of these assumptions is done in appendix B. It turns out that the errors calculated here are irrelevant compared to systematic errors when using the simplified

v [m/s]	Δv_l [m/s]	Δv_u [m/s]	h_l [mm]	h_u [mm]
4-5	0.008	0.015	96.7	99.67
5-6	0.016	0.027	99.69	101.3
6-7	0.027	0.043	101.31	102.28
7-8	0.043	0.064	102.29	102.92
8-9	0.064	0.090	102.93	103.35
9-10	0.091	0.125	103.36	103.67
10-11	0.125	0.166	103.67	103.9
11-12	0.166	0.214	103.9	104.07
12-13	0.217	0.273	104.08	104.21

Tab. 4: Calculated velocities for specific aperture heights. The errors shown derive from an error in the aperture height.

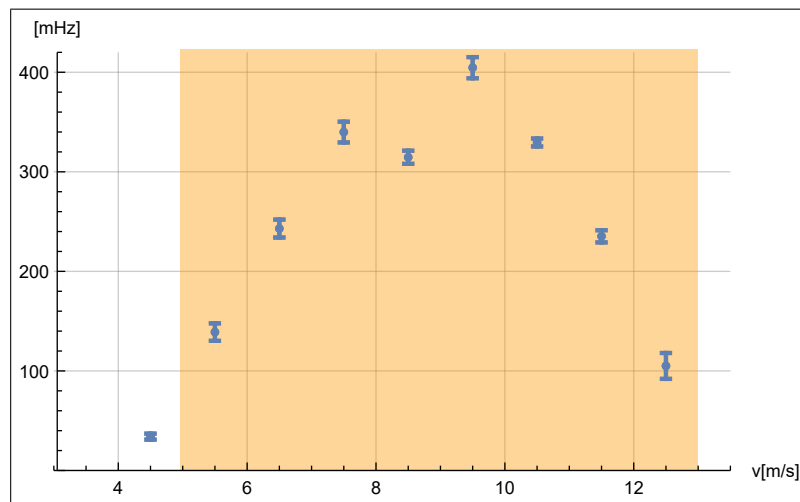


Fig. 15: Measured neutron rates, when using aperture slits to select a specific velocity interval. The orange area shows the velocity window selected for the final experiment.

v[m/s]	r [mHz]	Δr [mHz]	P[v]	ΔP [v]
4-5	34	3	0.015	0.001
5-6	139	8.8	0.064	0.003
6-7	243	9	0.113	0.003
7-8	339.9	10.41	0.158	0.004
8-9	314.6	6.6	0.146	0.003
9-10	404.6	10.6	0.188	0.004
10-11	329.45	4	0.153	0.002
11-12	235.2	6.1	0.109	0.002
12-13	105	13	0.048	0.005

Tab. 5: Velocities with measured count rates and calculated probabilities.

model of the flight parabola.

3.3 Region I and V

In Region I the neutrons from the aperture hit the first neutron mirror and propagate (“bounce”) on it. Above the mirror there is a glass absorber at a height of $\approx 23 \mu\text{m}$. The eigen energies of these neutrons is in the peV above the mirror surface and the Fermi energy of the mirror is in the 100 neV range. Therefore the overlap of neutron wave function and the mirror is negligibly small and the wave function can be assumed to vanish on the mirror surface. Higher energy neutrons have a wave function that extends farther above the mirror than low energy ones. These wave functions overlap with the absorber, so there is a probability of interacting with it. In this way high energy neutrons are scattered by the absorber and leave the interferometer. The absorber was first placed on $30 \mu\text{m}$ brass feeler gauges and then pressed down by two clamps. Four micrometer screws are used to accurately move the absorber down, deforming the feeler gauges, until the desired height is reached. The height calibration was performed by placing the absorber on the neutron mirror without the feeler gauges, then three linear gauges were referenced to this height. The absorber was lifted up, the feeler gauges inserted and the height was directly measured. With the three linear gauges the absorber could be placed as close to parallel as possible above the mirror. A picture of this process can be seen in fig. 16. The requirement to remove most of the higher energy neutrons from the system meant that the absorber should be placed $\approx 25 \mu\text{m}$ above the mirror. The final measured absorber height for region I was $l = (25.0 \pm 0.1) \mu\text{m}$ and for region V $l = (26.0 \pm 0.1) \mu\text{m}$. After the absorber was fixed on the mirror, the mirror height was adjusted to be $(105.0 \pm 0.1) \text{mm}$ above the granite surface. Each of these regions was then placed behind the aperture and the transmission rate was measured. Additionally, the slit between mirror and absorber was blocked by the aluminium sheet and the rate was measured. This was done to ensure that the background shielding is still effective even with the neutron mirrors in place and that the neutrons go through the slit. The

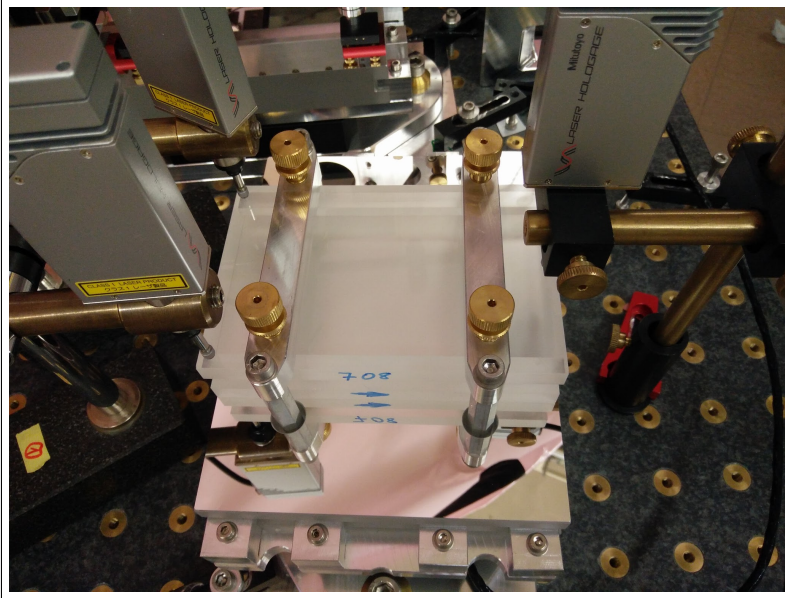


Fig. 16: Setup to calibrate the absorber above a neutron mirror.

Region	Rate	Background
I	(210.48 ± 3.75) mHz	(0.66 ± 0.66) mHz
I blocked	(0.59 ± 0.12) mHz	(0.73 ± 0.42) mHz
V	(220.77 ± 2.09) mHz	(0.63 ± 0.37) mHz
V blocked	(0.91 ± 0.24) mHz	(0 ± 0) mHz

Tab. 6: Transmission rates as measured behind regions I and V. With and without blocked path to check for background.

measured results can be seen in tab. 6. To confirm that the absorber works and indeed selects appropriate quantum states, a spatially resolving neutron detector, a coated CR-39 detector, was placed after the mirror and the neutron distribution in vertical direction was measured. By fitting theoretical neutron wave functions the distribution of neutrons can be inferred. The observed neutron distribution with the probabilities $P(\psi_n)$ for the different states can be seen in tab. 7. These detectors were analysed by Martin Thahammer.

3.4 Region II-IV

Regions II to IV also consist of a neutron mirror, but no absorber is placed above them. Because of this the preparation was less involved. Only the height was adjusted to the same as that of regions I and V. Regions II and IV are used to drive the transitions.

Region	$P(\psi_1)$	$P(\psi_2)$	$P(\psi_3)$
I	0.52	0.37	0.10
V	0.46	0.43	0.11

Tab. 7: Measured Distribution of states behind Region I and V.

Because of this special care was taken to avoid contact with the neighbouring regions. This was done by using feeler gauges to move them as close together as possible. After regions I and V were prepared, region two was inserted between them and basic Rabi transition measurements were performed. An analysis of these measurements can be found in chapter 3.6. After these the full Ramsey spectrometer was built with all five regions. In addition the steps between the mirrors were measured with linear gauges to reduce unwanted steps. These would lead to an additional neutron loss which would increase measurement time. After this initial setup by hand the mirror steps were measured by separate capacitive sensor which keep the mirrors level.

3.5 Leveling

The capacitive sensors are held by an aluminium structure and can be moved along the mirror. Using the capacitive sensors, the mirror height is continually adjusted to remain stable and to compensate steps, caused by a mirror drift. There are four sensors over the regions and three more sensors over an additional reference mirror. The final spectrometer setup can be seen in fig. 17. The additional sensors a, b and p are used to reference the rest of the sensors to a common plane. This is necessary because the aluminium structure can warp during the movements of the sensors and the sensors over the regions would measure a changing mirror position. The reference mirror under a,b and p does not move and is therefore always level. With an established reference frame the neutron mirrors can then be adjusted to this plane and kept there. During one measurement the adjustment was done continually. The height measurement was problematic and could not be calibrated during the experiment time. In theory the sensors would have given enough information to adjust the mirror positioning so that there are little to no steps, but the combination of sensors and mirrors in this configuration could not be sufficiently analysed. The steps between mirrors could not be reliably eliminated and the inclination of the mirrors could not be controlled accurately. Later we found out, that the surface of the reference mirror used for calibration was not sufficiently flat and disturbed the measurement. To compensate the neutron mirrors were adjusted by hand to be as close to flat as possible. The height profile was then measured using the capacitive sensors. To ensure stability for future measurements, this height profile was saved and all future height measurements were adjusted, so that the mirrors remained at their initial position over the course of a measurement.

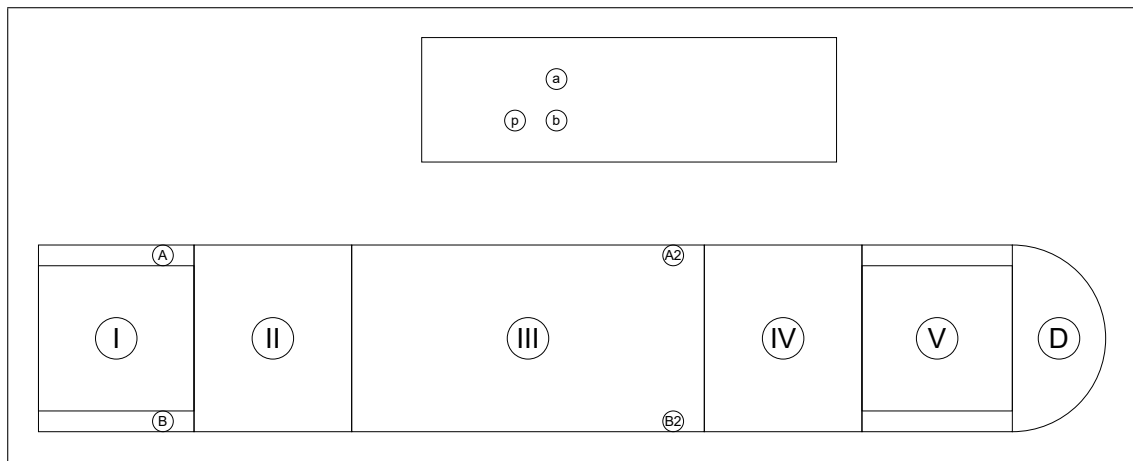


Fig. 17: Final setup of the Ramsey spectrometer. The sensors A, B, A2, B2 are used to check the region mirrors and the sensors a, b and p above a reference mirror are used to reference all other measurements to a common plane.

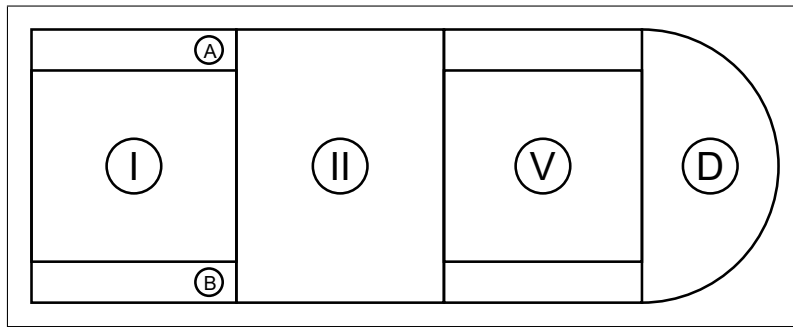


Fig. 18: Setup of the Rabi experiment. Neutrons enter from the left into Region I with an absorber, Region II is inducing transitions, Region III selects the final state, the detector D detects transmitted neutrons and the two sensors A and B measure the position of all the mirrors during a measurement.

3.6 Rabi setup

Using the Rabi spectrometer section of the Ramsey spectrometer, briefly described in section 3.4, a preliminary measurement was carried out. The setup for this measurement can be seen in fig. 18. The neutrons enter from the left, where the slit aperture is located. Then region I selects neutrons in the ground state, and region II induces transitions with oscillations. Then in region V the neutrons in the ground state are again selected and detected in the detector D. The capacitive sensors A and B are used to monitor the height of the neutron mirrors, with the goal that no steps are between the regions. They can move over all three regions. the reference sensors a, b and p are not show, but they are used for leveling.

3.6.1 Driving transitions in the Rabi setup

Region II is oscillated to induce transitions between states. The transition of choice was from the ground state to the second excited state. This transition was chosen, because the third state is reasonably unpopulated, as shown in 7, and the transition frequency is low. The theoretical transition frequency is calculated in section 2.1 and is given by $f = 462.925$ Hz. The velocity of the oscillation was chosen to be $a\omega \approx 1.6$ mm/s. Using the distribution of states given in tab. 7 and equation (19) the expected transmission spectrum can be calculated. The numerical solution of this system can be seen in fig. 19, where the first four energy eigenstates and the velocity distribution of the system were considered.

3.6.2 Measurements and Results

A series of measurements was performed, both while oscillating region II and without oscillation to check for the baseline transmission. The measured data can be seen in fig. 20, where the zero rate measurements are in blue and the measurements during

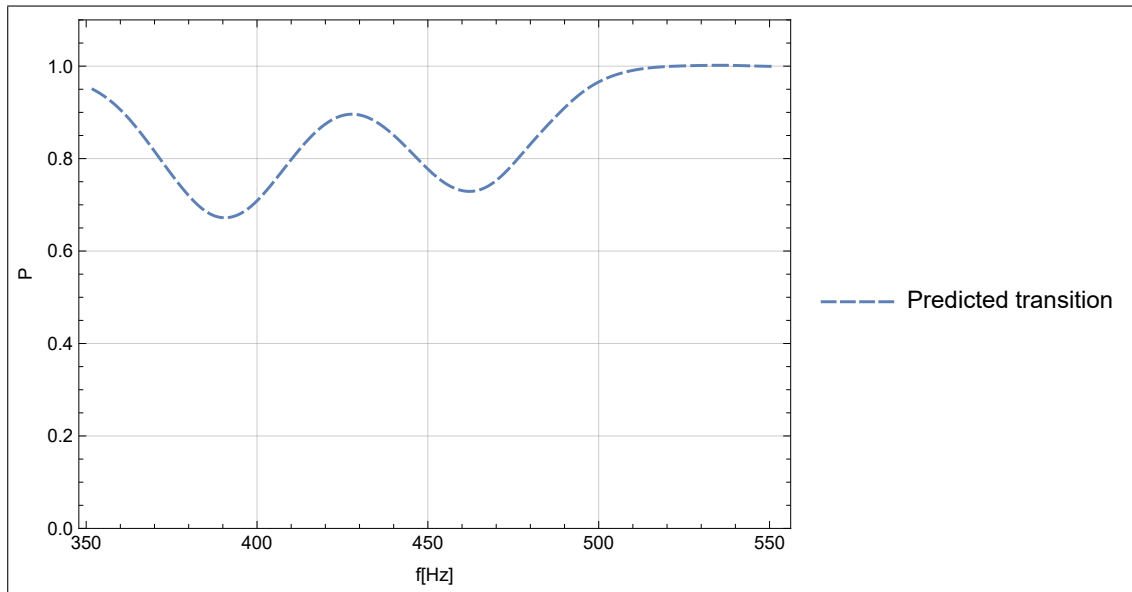


Fig. 19: Simulated transition, when taking the velocity distribution and the first four energy eigenstates into account.

oscillations in orange. The zero rate is dropping because of contamination of the vacuum. This gradual decrease has also been observed in following measurements and was later found to follow an approximate exponential decrease and was caused by oil from motors inside the vacuum chamber. These motors were subsequently replaced.

The varying neutron rate from the UCN source was compensated by referencing the measurements to an external neutron detector in front of the vacuum chamber. The final dataset referenced to the external neutron rate can be seen in fig. 21, where the solid line is an exponential fit to the zero rate measurements. The oscillations suffered from additional systematic effects, which could not be compensated in data analysis.

Since these measurements were done during the setup of the Ramsey spectrometer, no detailed corrections or repeated measurements were possible. The theoretical curve was not known at the time of the experiment. Therefore the measured frequencies were chosen without consideration of the second dip at $f = 392.566$ Hz shown in 19. This dip is a result from considering more than two states, as assumed in the ideal Rabi transition from the first to the third eigen state, in this case the transition from the second to the fourth state (this frequency can be found in tab. 2).

With the available measurements, no statement can be made about quantum mechanical effects, since the reduced transition rates in fig. 20 could be the result of systematic errors unknown at the time of the measurement. With additional measurements a Rabi transition could have been observed, but these measurements were foregone in favour of extending the experimental setup to the full Ramsey spectrometer.

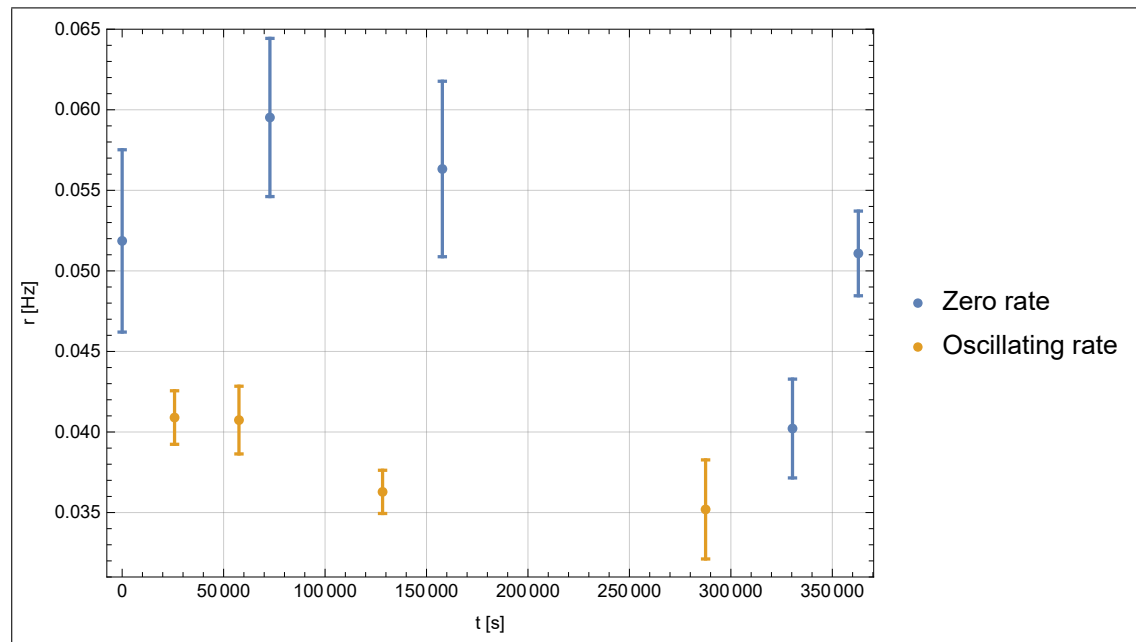


Fig. 20: Measured rates during the Rabi spectroscopic measurements. The time axis is shown from the first measurement.

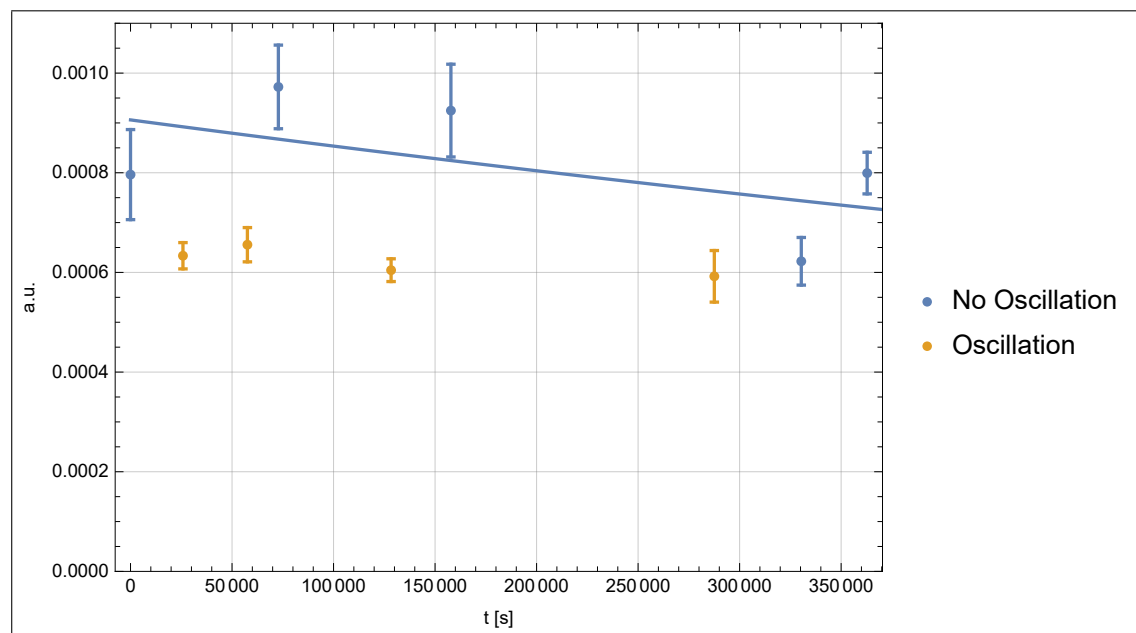


Fig. 21: Final cleaned dataset.

4 Conclusio

During this master thesis the set up of the first Gravity Resonance Spectrometer with UCNs using the Ramsey method was supervised. The components of the spectrometer were separately tested and aligned (section 3). Previous measurements, using the Rabi method, were also replicated (section 3.6). These measurements were inconclusive, because time constraints didn't allow for statistically significant measurements. With the completed Ramsey spectrometer measurements were performed for the first time. These suffered from systematic effects. Especially the adjustment of the individual mirror heights was problematic due to an uneven reference mirror. This mirror was replaced by a new one with a measured surface (section 3.5). In addition, the selection of an appropriate transition was difficult because of the uncertainties in the initial state due to the absorber (section 3.3). The comparison with theoretical predictions is also complicated by the fact that the velocity spectrum of the neutrons is not known accurately (section 3.2). After the first measurements in 2017 improvements to the setup have been made to address these issues and to reduce the systematic effects with improved measurements under way.

References

- [1] Valery V. Nesvizhevsky, Hans G. Börner, Alexander K. Petukhov, Hartmut Abele, Stefan Baessler, Frank J. Ruesz, Thilo Stoferle, Alexander Westphal, Alexei M. Gagarski, Guennady A. Petrov, and Alexander V. Strelkov. Quantum states of neutrons in the earth's gravitational field. *Nature*, 415(6869):297–299, January 2002.
- [2] V. V. Nesvizhevsky, H. G. Börner, A. M. Gagarski, A. K. Petoukhov, G. A. Petrov, H. Abele, S. Baeßler, G. Divkovic, F. J. Rueß, Th. Stöferle, A. Westphal, A. V. Strelkov, K. V. Protasov, and A. Yu. Voronin. Measurement of quantum states of neutrons in the earth's gravitational field. *Phys. Rev. D*, 67:102002, May 2003.
- [3] R. Golub, D. Richardson, and S.K. Lamoreaux. *Ultra-Cold Neutrons*. Taylor & Francis, 1991.
- [4] V.I. Luschikov and A.I. Frank. Quantum effects occurring when ultra cold neutrons are stored on a plane. *Joint Institute for Nuclear Research*, 1978.
- [5] Katharina Durstberger-Rennhofer, Tobias Jenke, and Hartmut Abele. Probing neutron's electric neutrality with Ramsey Spectroscopy of gravitational quantum states of ultra-cold neutrons. *Phys. Rev.*, D84:036004, 2011.
- [6] T. Jenke, David Stadler, Hartmut Abele, and Peter Geltenbort. Q-bounce—experiments with quantum bouncing ultracold neutrons. 611:318–321, 12 2009.
- [7] H. Abele, T. Jenke, D. Stadler, and P. Geltenbort. Qubounce: the dynamics of ultra-cold neutrons falling in the gravity potential of the earth. *Nuclear Physics A*, 827(1):593c – 595c, 2009. PANIC08.
- [8] H. Abele, G. Cronenberg, P. Geltenbort, T. Jenke, T. Lins, and H. Saul. qbounce, the quantum bouncing ball experiment. *Physics Procedia*, 17(Supplement C):4 – 9, 2011. 2nd International Workshop on the Physics of fundamental Symmetries and Interactions - PSI2010.
- [9] Martin Thalhammer. *TBP*. PhD thesis, Vienna University of Technology, 2018.
- [10] Tobias Jenke, Gunther Cronenberg, Hanno Filter, Peter Geltenbort, Martin Klein, Thorsten Lauer, Kevin Mitsch, Heiko Saul, Dominik Seiler, David Stadler, Martin Thalhammer, and Hartmut Abele. Ultracold neutron detectors based on 10b converters used in the qbounce experiments. *Nuclear Instruments and Methods in Physics Research Section A: Accelerators, Spectrometers, Detectors and Associated Equipment*, 732:1 – 8, 2013. Vienna Conference on Instrumentation 2013.
- [11] Tobias Jenke, Peter Geltenbort, Hartmut Lemmel, and Hartmut Abele. Realization of a gravity-resonance-spectroscopy technique. *Nature Physics*, 7:468, April 2011.

-
- [12] Norman F. Ramsey. A molecular beam resonance method with separated oscillating fields. *Phys. Rev.*, 78:695–699, Jun 1950.
 - [13] Gunther Cronenberg. *Frequency measurements testing Newton’s Gravity Law with the Rabi-qBounce experiment*. PhD thesis, Vienna University of Technology, 2015.
 - [14] O. Vallée and M. Soares. *Airy Functions and Applications to Physics*. EBSCO ebook academic collection. World Scientific, 2004.
 - [15] H. Abele, T. Jenke, H. Leeb, and J. Schmiedmayer. Ramsey’s method of separated oscillating fields and its application to gravitationally induced quantum phase shifts. *Phys. Rev. D*, 81:065019, Mar 2010.
 - [16] Tobias Jenke. *qBOUNCE - vom Quantum Bouncer zur Gravitationsresonanzspektroskopie*. PhD thesis, Vienna University of Technology, 2011.

A Airy functions

Here I will derive solutions to the Airy differential equation

$$y'' - zy = 0, \quad (34)$$

In particular both real valued Airy functions Ai and Bi are found, in accordance with [14]. As an ansatz for the solution,

$$y(z) = \int_C f(s) e^{sz} ds \quad (35)$$

is taken, where C is some path in the complex plane. Depending on the choice for C, different solutions are found. The paths I used to calculate the solutions here were found without considering literature and lead to the usual integral representations of the Airy functions. Inserting this ansatz in (34) gives

$$\begin{aligned} \Rightarrow \int_C (f(s)s^2 - zf(s)) e^{sz} ds &= \int_C \left(f(s)s^2 - f(s) \frac{\partial}{\partial s} \right) e^{sz} = \\ &\int_C \left(f(s)s^2 e^{sz} - \frac{\partial}{\partial s} (f(s)e^{sz}) + \frac{\partial}{\partial s} (f(s)) e^{sz} \right) ds = \\ &\int_C (f(s)s^2 + f'(s)) e^{sz} ds - \int_C \frac{\partial}{\partial s} (f(s)e^{sz}) ds = \\ &\int_C (f(s)s^2 + f'(s)) e^{sz} ds - [(f(s)e^{sz})]_C = 0. \end{aligned} \quad (36)$$

If the path C is chosen such that

$$[(f(s)e^{sz})]_C = 0, \quad (37)$$

then $f(s)$ has to satisfy

$$f'(s) + f(s)s^2 = 0. \quad (38)$$

A solution to this equation is given by $f = e^{-\frac{s^3}{3}}$. Inserting this in the condition in (37) results in

$$[(f(s)e^{sz})]_C = \left[e^{-\frac{s^3}{3} + sz} \right]_C = 0. \quad (39)$$

Since the function does not have any zeroes in the complex plane, the simplest choice are closed paths to satisfy this condition. However, the integrand in (35) has no singularities, so the integral vanishes for all closed paths. The solution is the zero solution. To find non zero solutions the path must not be closed. This can be fulfilled, by choosing the endpoints of the path C so that

$$\Re(s^3) > 0 \text{ as } |s| \rightarrow \infty. \quad (40)$$

With this condition (37) is fulfilled. Taking the complex variable $s = |s|e^{i\varphi}$, with $\varphi \in [0, 2\pi]$ leads to

$$\Re(s^3) = \Re(|s|^3 e^{i3\varphi}) > 0 \Rightarrow \cos(3\varphi) > 0 \Rightarrow \varphi \in \begin{cases} [-\frac{\pi}{6}, \frac{\pi}{6}] \\ [\frac{3\pi}{6}, \frac{5\pi}{6}] \\ [\frac{7\pi}{6}, \frac{9\pi}{6}] \end{cases}. \quad (41)$$

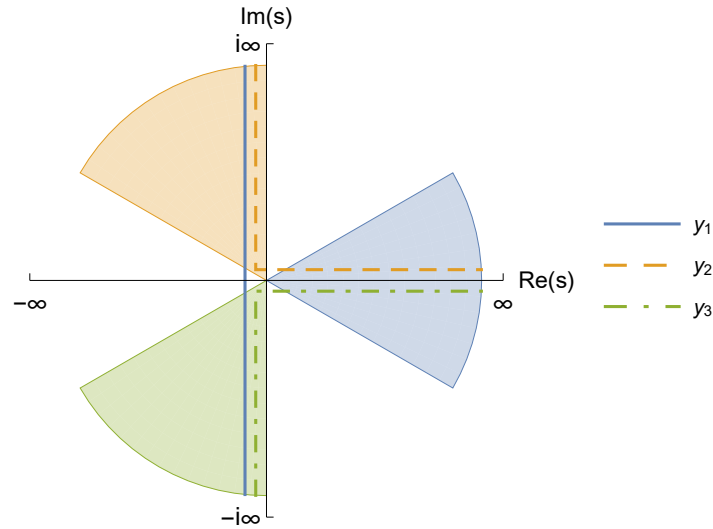


Fig. 22: In colour are the regions in which the path C fulfills condition (37). y_1 , y_2 and y_3 are three specific choices for the paths. The paths shown run on top of the axes.

The three regions are shown in fig. 22. Any path that connects two different regions leads to a solution. A path that enters from one and exits in the same region again leads to the zero solution, because it can be closed at infinity, where the integrand goes to 0. There are three different paths connecting two regions, so there are three different solutions given by equation (35). However, since (34) is a second order linear differential equation, there are only two linearly independent solutions. The three solutions y_1 , y_2 , y_3 also satisfy

$$y_1 + y_2 + y_3 = \oint e^{-\frac{s^3}{3} + sz} ds = 0, \quad (42)$$

since the sum of the integrals leads to an integral along a closed path, which is zero. One choice of three different paths is also shown in fig. 22 and the corresponding solutions are given by

$$y_1 = \int_{-i\infty}^{i\infty} e^{-\frac{s^3}{3} + sz} ds \quad (43)$$

$$y_2 = \int_{i\infty}^{\infty} e^{-\frac{s^3}{3}+sz} ds \quad (44)$$

$$y_3 = \int_{\infty}^{-i\infty} e^{-\frac{s^3}{3}+sz} ds \quad (45)$$

From these, the Airy functions can be constructed. From (43) follows that

$$y_1 = \int_{-i\infty}^{i\infty} e^{-\frac{s^3}{3}+sz} ds \stackrel{s \rightarrow is}{=} i \int_{-\infty}^{\infty} e^{i\left(\frac{s^3}{3}+sz\right)} ds, \quad (46)$$

which is proportional to the solution in the main text in equation (??). This can be further simplified by

$$\begin{aligned} y_1 &= i \left(\int_{-\infty}^0 e^{i\left(\frac{s^3}{3}+sz\right)} ds + \int_0^{\infty} e^{i\left(\frac{s^3}{3}+sz\right)} ds \right) = \\ & i \left(\int_0^{\infty} e^{-i\left(\frac{s^3}{3}+sz\right)} ds + \int_0^{\infty} e^{i\left(\frac{s^3}{3}+sz\right)} ds \right) = \\ & i \int_0^{\infty} \left(e^{-i\left(\frac{s^3}{3}+sz\right)} + e^{i\left(\frac{s^3}{3}+sz\right)} \right) ds = \\ & 2i \int_0^{\infty} \cos\left(\frac{s^3}{3} + sz\right) ds = \\ & 2\pi i \frac{1}{\pi} \int_0^{\infty} \cos\left(\frac{s^3}{3} + sz\right) ds = 2\pi i \text{Ai}(z). \end{aligned} \quad (47)$$

This equation defines the Airy-function Ai as

$$\text{Ai}(z) = \frac{1}{\pi} \int_0^{\infty} \cos\left(\frac{s^3}{3} + sz\right) ds. \quad (48)$$

Similarly y_2 can be written as

$$\begin{aligned} y_2 &= \int_0^{\infty} e^{-\frac{s^3}{3}+sz} ds + \int_{i\infty}^0 e^{-\frac{s^3}{3}+sz} ds = \int_0^{\infty} e^{-\frac{s^3}{3}+sz} ds - i \int_0^{\infty} e^{i\left(\frac{s^3}{3}+sz\right)} ds = \\ & \int_0^{\infty} \left(e^{-\frac{s^3}{3}+sz} - i e^{i\left(\frac{s^3}{3}+sz\right)} \right) ds, \end{aligned} \quad (49)$$

and y_3 as

$$y_3 = \int_0^{\infty} \left(-e^{-\frac{s^3}{3}+sz} - i e^{-i\left(\frac{s^3}{3}+sz\right)} \right) ds \quad (50)$$

Adding these two solutions leads to

$$y_2 + y_3 = -2i\pi \text{Ai}(z), \quad (51)$$

which is again proportional to the already known solution. Also the fact that $y_1 + y_2 + y_3 = 0$ is evident. On the other hand

$$\begin{aligned}
 y_2 - y_3 &= \int_0^\infty \left(2e^{-\frac{s^3}{3}+sz} - i \left(e^{i\left(\frac{s^3}{3}+sz\right)} - e^{-i\left(\frac{s^3}{3}+sz\right)} \right) \right) ds = \\
 &\int_0^\infty \left(2e^{-\frac{s^3}{3}+sz} - 2i^2 \sin \left(\frac{s^3}{3} + sz \right) \right) ds = \\
 &\int_0^\infty \left(2e^{-\frac{s^3}{3}+sz} + 2 \sin \left(\frac{s^3}{3} + sz \right) \right) ds = \\
 &2\pi \frac{1}{\pi} \int_0^\infty \left(e^{-\frac{s^3}{3}+sz} + \sin \left(\frac{s^3}{3} + sz \right) \right) ds = 2\pi \text{Bi}(z),
 \end{aligned} \tag{52}$$

where

$$\text{Bi}(z) = \frac{1}{\pi} \int_0^\infty \left(e^{-\frac{s^3}{3}+sz} + \sin \left(\frac{s^3}{3} + sz \right) \right) ds \tag{53}$$

Thus the three paths give

$$y_1 = 2\pi i \text{Ai}(z) \tag{54}$$

$$y_2 = \pi(\text{Bi}(z) - i\text{Ai}(z)) \tag{55}$$

$$y_3 = -\pi(\text{Bi}(z) + i\text{Ai}(z)) \tag{56}$$

and the two real Airy-functions are given by

$$\text{Ai}(z) = \frac{y_1}{2\pi i} = \frac{1}{\pi} \int_0^\infty \cos \left(\frac{s^3}{3} + sz \right) \tag{57}$$

$$\text{Bi}(z) = \frac{y_2 - y_3}{2\pi} = \frac{1}{\pi} \int_0^\infty \left(e^{-\frac{s^3}{3}+sz} + \sin \left(\frac{s^3}{3} + sz \right) \right) ds . \tag{58}$$

These two solutions are the two Airy-functions shown in fig. 4.

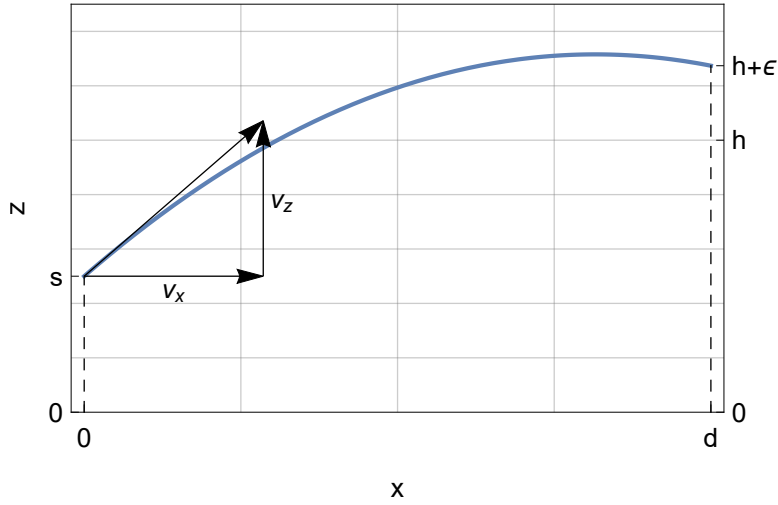


Fig. 23: A classical flight parabola. The height at position $x = 0$ is $z(0) = s$ and at $x = d$, $z(d) = h + \epsilon$. The height of the absorber is not shown and is given by $h + l$. The traveled height is given by $z(d) - s = h - s + \epsilon$

B Slit aperture and flight parabola

In this section I will explain how the aperture setup, also described in section ??, limits the velocity in flight direction of the UCNs. This is a purely classical description and problems with this approach are addressed. The quantum mechanical description faces its own problems and will not be described here.

For the calculation, the neutrons are assumed to be point particles, flying in x -direction and experiencing the gravitational acceleration $a = -g$ in z -direction. The equations of motion are

$$x(t) = v_x t, \quad z(t) = s + v_z t - \frac{g}{2} t^2, \quad v_z(t) = v_z - gt, \quad (59)$$

where s is the height at position $x = 0$, v_x is the velocity in the x -direction and v_z is the velocity in z -direction at time $t = 0$. The function $v_z(t)$ is the velocity at arbitrary times t . Eliminating $t = x/v_x$ leads to

$$z(x) = s + \frac{v_z}{v_x} x - \frac{g}{2v_x^2} x^2, \quad v_z(x) = v_z - \frac{g}{v_x} x \quad (60)$$

In fig. 23 a flight path is shown. s is the height of the flight path at the aperture, h is the height of the mirror, d is the distance of the mirror to the aperture, and ϵ is the height of the flight path above the mirror. Defining the vertical velocity at d as α results in

$$v_z(d) = \alpha = v_z - \frac{g}{v_x} d \Rightarrow v_z = \alpha + \frac{gd}{v_x}. \quad (61)$$

Assuming the absorber is a distance l above the mirror, and that the neutron passes at a height of ϵ above the mirror, the velocity α can be constrained by requiring that the

kinetic energy is lower than the remaining potential energy to reach the absorber. α is then constrained to

$$\frac{m\alpha^2}{2} \leq mg(l - \epsilon) \Rightarrow \alpha^2 \leq 2g(l - \epsilon) \Rightarrow \alpha \in \left[-\sqrt{2g(l - \epsilon)}, \sqrt{2g(l - \epsilon)} \right]. \quad (62)$$

Inserting α into eq. (60) gives

$$v_z(x) = \alpha + \frac{g}{v_x}(d - x) \quad (63)$$

$$z(x) = \frac{\alpha}{v_x}x + \frac{gd}{v_x^2}x - \frac{gx^2}{2v_x^2} = \frac{\alpha}{v_x}x + \frac{g}{2v_x^2}x(2d - x). \quad (64)$$

The constraint that $z(d) - s = h - s + \epsilon$ gives

$$z(d) = \frac{\alpha}{v_x}d + \frac{g}{2v_x^2}d^2 = h - s + \epsilon \Rightarrow v_x^2 - \frac{\alpha d}{h - s + \epsilon}v_x - \frac{gd^2}{2(h - s + \epsilon)} = 0 \quad (65)$$

$$v_x = \frac{\alpha d}{2(h - s + \epsilon)} + \sqrt{\frac{\alpha^2 d^2}{4(h - s + \epsilon)^2} + \frac{gd^2}{2(h - s + \epsilon)}}, \quad (66)$$

where only the plus sign is relevant, since the neutrons are supposed to move in the positive x -direction.

With this expression, a velocity distribution can be obtained by sampling the parameters α , s and ϵ . Two examples of this can be seen in fig. 24, where a uniform distribution of all three parameters is assumed. The blue histograms show the simulation with zero absorber height and the orange histogram with 100 μm , as was used in the measurements. The biggest uncertainty with this approach is that the parameters are probably not uniformly distributed. s should be sampled with the spatial distribution at the slit aperture and α and ϵ are both dependent on the velocity distribution in z -direction at the aperture, which can also be z dependent. But since neither the spatial nor the velocity distribution in z -direction are known, the only way to reconstruct the velocity distribution is to take these assumptions and compare them with the measurements described in section 3.2. As can be seen in fig. 25, the results of the piecewise measurements are not compatible with the predictions of the simulated model. Therefore the unknown distributions and other systematic effects are not properly taken into account by the used assumptions. Making further guesses about the velocity and spatial distributions is not justified, since no simple model can reproduce the two peak structure measured. Adding weights following a normal distribution to the simulation results in the green data points in the plot. This assumption can not accurately reproduce the measured distribution. At this point the only reasonable thing to do is to take the measurements as given and use the simple model from the main text as a guideline, since no gain results from the more complex model presented here.

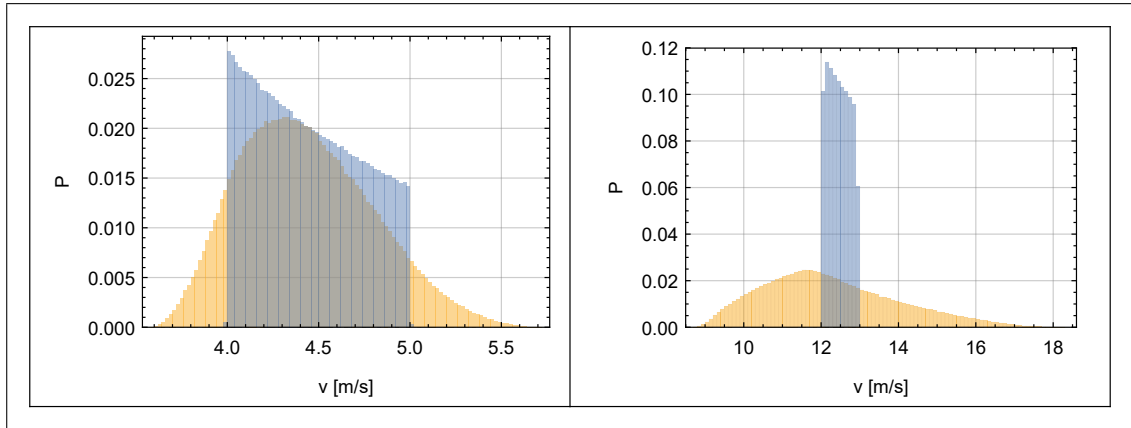


Fig. 24: Simulated velocity spectra. In blue the simulation for absorber height of zero, and in orange an absorber height of $100\ \mu\text{m}$.

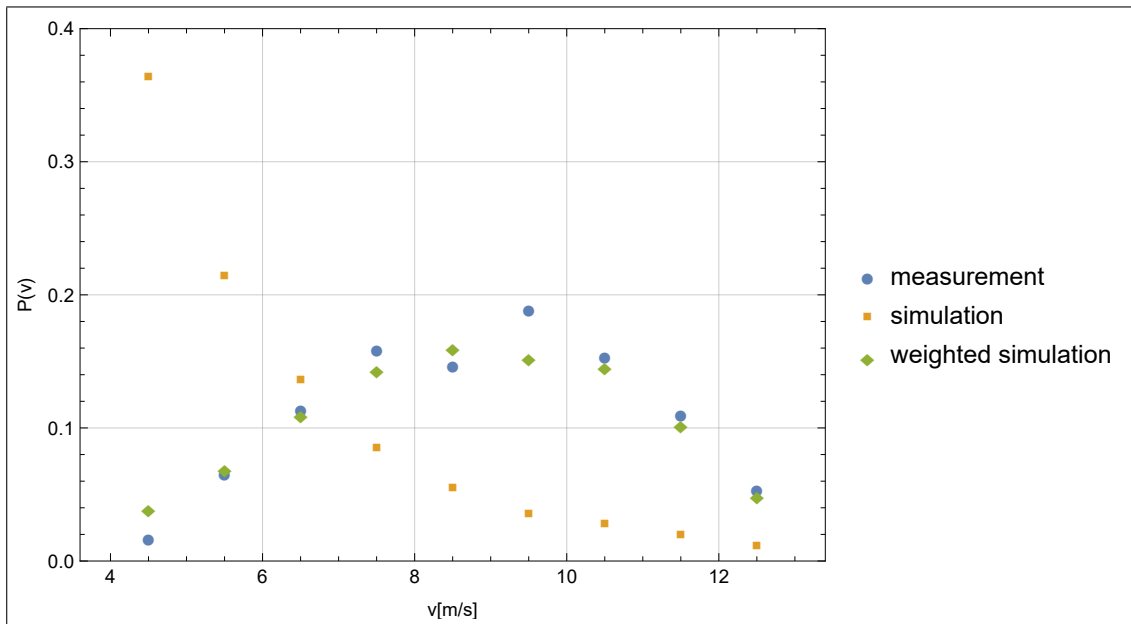


Fig. 25: Comparison of the total simulated spectrum, in orange, with the measured spectrum, in blue. In green is the simulation weighted according to a normal distribution.